

Loughborough University  
Wolfson School of Mechanical, Electrical  
and Manufacturing Engineering

**Recycling inert gases for plasma-assisted  
carbon dioxide splitting using a split-ring  
resonator**

Prateep Ganesh Kasinathan

1<sup>st</sup> March 2023



# Contents

<b>1</b>	<b>Introduction</b>	<b>1</b>
1.1	Motivation . . . . .	1
1.2	Novelty . . . . .	2
<b>2</b>	<b>Plasma Overview</b>	<b>4</b>
2.1	Plasma Discharge . . . . .	4
2.1.1	Paschen's Law . . . . .	5
2.1.2	DC Discharge . . . . .	7
2.1.3	AC Discharge . . . . .	10
<b>3</b>	<b>Carbon Dioxide Splitting</b>	<b>12</b>
3.1	Traditional Process . . . . .	12
3.2	Plasma-assisted $CO_2$ Splitting . . . . .	15
<b>4</b>	<b>Split Ring Resonator</b>	<b>17</b>
4.1	Overview . . . . .	18
4.2	Production . . . . .	19

4.2.1	Simulations . . . . .	19
4.2.2	Design . . . . .	24
4.3	Testing . . . . .	25
<b>5</b>	<b>Epoxidation Process</b>	<b>28</b>
<b>6</b>	<b>Gas recirculation</b>	<b>29</b>
<b>7</b>	<b>Conclusion</b>	<b>30</b>
<b>A</b>	<b>Particle-in-Cell Simulations</b>	<b>31</b>
A.1	Particle Mover . . . . .	33
A.2	Charge and Current Deposition . . . . .	36
A.3	Field Solver . . . . .	37
A.4	Field Interpolation . . . . .	40
A.5	Monte-Carlo Collisions . . . . .	41
<b>B</b>	<b>XOOPIC</b>	<b>43</b>
B.1	Overview . . . . .	43
B.1.1	Remote Server . . . . .	44
B.1.2	Input Files . . . . .	45
B.2	Improvements . . . . .	46
B.2.1	Motivation . . . . .	46
B.2.2	Methodology . . . . .	48

B.2.3	Validation . . . . .	53
B.2.4	Future Work . . . . .	59

<b>Bibliography</b>		<b>59</b>
---------------------	--	-----------



# List of Tables

4.1	Simulation parameters of SSR in XOOPIC. . . . .	20
A.1	Determining the type of collision based on the value of $R$ [35]. . . . .	42
B.1	Circuit boundary variables for cartesian geometry. . . . .	52
B.2	Circuit boundary variables for cylindrical geometry. . . . .	53
B.3	Parameters for test case of Circuit boundary without particles. . . . .	54
B.4	Parameters for test case of Circuit boundary with particles. . . . .	57





# List of Figures

1.1	Global greenhouse gas emissions by sector [3]. . . . .	2
2.1	Paschen curve for Helium, Neon, Argon, Hydrogen, and Nitrogen gases [6]. . . .	6
2.2	Circuit diagram with a source voltage ( $V_s$ ) and variable resistor ( $R$ ) to control the current through a discharge region ( $C$ to $A$ ) [7]. . . . .	7
2.3	Depiction of the current-voltage relationship across three discharge regions [8]. .	8
2.4	Schematic highlighting the regions present in a DC glow discharge [9]. The cathode is on the left and the grounded anode is on the right. (CDS is the cathode dark space, NG is the negative glow, and AZ is the anode dark space. .	9
2.5	Paschen curve for AC discharge across various frequencies [12]. . . . .	11
3.1	Gibbs free energy of formation for different chemicals based on data from the NIST database. [14] . . . . .	13
3.2	Thermal conversion and energy efficiency of $\text{CO}_2$ splitting as a function of temperature. [15] . . . . .	13
3.3	Schematic of microwave reactors for $\text{CO}_2$ splitting. [15] . . . . .	15
4.1	Schematic (left) and photo (right) of SRR [21]. . . . .	17
4.2	A comparison of SSR with and without hole in gap. . . . .	20

4.4	Time series plot of number of electrons across different discharge gaps. . . . .	22
4.6	PCB design of SSR in KiCad. . . . .	26
A.1	Process flow of PIC simulations. . . . .	32
A.2	Illustration of forward-difference and central-difference form [27]. . . . .	34
A.3	Visualisation of velocity rotation from the Boris algorithm [28]. . . . .	35
A.4	Interpolation from the grid to the particles [30]. . . . .	36
A.5	Illustration of ADI method [32]. . . . .	39
A.6	Addition of null collision to produce a constant collision frequency across all energies [35]. . . . .	42
B.1	Illustration of circuit boundary. . . . .	47
B.2	Voltage-current relationship of circuit boundary. . . . .	48
B.3	Illustration of a circuit boundary along a fixed grid. . . . .	49
B.4	Illustration of test case for Circuit boundary without particles. . . . .	54
B.5	Comparison between the analytical solution and XOOPIC, where $\Delta t = 10$ ps. . .	55
B.6	Comparison between the analytical solution and XOOPIC, where $\Delta t = 1$ ns. . .	55
B.7	Comparison of the error from XOOPIC when $\Delta t = 10$ ps and $\Delta t = 1$ ns. . . .	56
B.8	Illustration of test case for Circuit boundary without particles. . . . .	56
B.9	Illustration of test case for Circuit boundary without particles. . . . .	59

# Chapter 1

## Introduction

Anthropogenic climate change is a real problem and has been stated as “a threat to human well-being and the health of the planet” by the Intergovernmental Panel on Climate Change (IPCC) [1]. The driving force behind climate change has to do with the emissions of green house gases into the atmosphere. According to data from the United States Environmental Protection Agency, carbon dioxide ( $\text{CO}_2$ ) accounts for nearly three quarters of those greenhouse emissions [2]. A breakdown of emissions by sector can be seen in figure 1.1.

As seen in figure 1.1, global greenhouse emissions come from a variety of sources and processes. Hence, simply focusing efforts in areas such as transport or electricity generation is insufficient. Eliminating our dependance on fossil fuels by switching to renewables or driving electric cars is a start, but in order to achieve net-zero emissions, there needs to be innovations across various other sectors. Currently, there is no one solution to climate change.

### 1.1 Motivation

Now, supposing that we have successfully decarbonised the economy, there will always be industrial processes that produce  $\text{CO}_2$  as a byproduct. The quintessential example of this is the manufacturing of concrete, where the  $\text{CO}_2$  is released from a chemical process due to

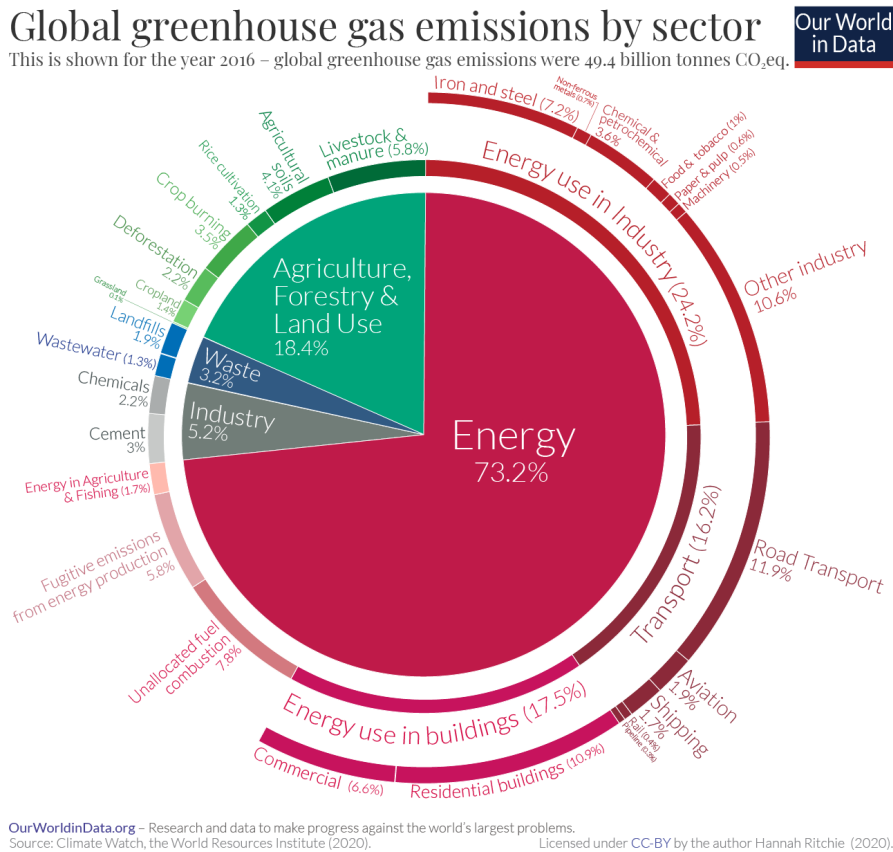


Figure 1.1: Global greenhouse gas emissions by sector [3].

the conversion of calcium carbonate ( $\text{CaCO}_3$ ) to calcium oxide ( $\text{CaO}$ ), rather than through combustion. As such it would be useful to capture this  $\text{CO}_2$  and potentially reuse it in other manufacturing processes.

There have many different approaches in the literature, with recent examples including generating synthetic fuels using electrochemical  $\text{CO}_2$  recycling [4] and using algae to convert  $\text{CO}_2$  into carbon fibre [5]. This report will specifically focus on the area of carbon conversion via  $\text{CO}_2$  splitting; specifically, plasma-assisted  $\text{CO}_2$  splitting.

## 1.2 Novelty

Plasma-assisted  $\text{CO}_2$  splitting is a relatively new technology that could be used for the process carbon conversion. In order to generate and sustain this plasma, inert feed gases (typically argon or helium) are oftentimes required. While the use of these feed gases are perfectly viable

in a research laboratory setting, when it comes to scaling the process to an industrial level, the costs associated become untenable.

The novelty with this project is to assess the viability of a plasma driven carbon utilisation process that recirculates the feed gas, reducing the cost associated with the use of inert gases. This would require a control system to maintain the pressure of the feed gas as there will inevitably be some losses. It would also require the filtration of any waste products produced from the CO<sub>2</sub> splitting process and subsequent chemical reactions.

The rest of this report is structured as follows. A introduction of plasma discharges can be found in chapter 2. Chapter 3 goes on to provide an overview of the CO<sub>2</sub> splitting process. Then, chapter 4 provides a description of the process to design and develop the plasma reactor used for this project, along with some basic tests using only Helium gas. CO<sub>2</sub> gas is then introduced to the plasma reactor in chapter 5, where the results from the CO<sub>2</sub> splitting process can be found. Chapter 6 goes on to describe the mechanism of waste filtration and feed gas recirculation. Finally, the results of this report are discussed in the conclusion.

# Chapter 2

## Plasma Overview

Plasma is a fundamental state of matter, along with solid, liquid, and gas. It has similar characteristics to gases, where it is compressible and does not conform to a specific shape; however the key difference is that plasmas are highly electrically conductive, even capable of producing their own magnetic field. This is because plasmas contain a large number of positive ions that interact in a ‘sea’ of free-moving electrons.

### 2.1 Plasma Discharge

Plasmas are generated in one of two primary ways. The first is via extreme heating of a gas whereby the electrons gain sufficient energy to escape the electromagnetic force of the nucleus. The most obvious example of this is in stars where the gases within reach temperatures millions of degrees Kelvin, giving rise to nuclear fusion. The other method, which is the main focus of this report, is the exposure of a gas to a large electric field. This in turn ignites the plasma in a process described in the rest of this chapter. An everyday example of this is lightning, where charges build up between the clouds and the ground, which in turn causes the potential difference between the two to grow until the air in between breaks down.

### 2.1.1 Paschen's Law

The voltage necessary to break down a gas is given by Paschen's law. It states that the breakdown voltage is a function of two parameters [6]: the pressure of the gas and the distance between the electrodes (referred to as the gap length). Specifically, the breakdown voltage is given by the product of these two parameters.

In order for breakdown to occur, there needs to be a small number of electrons already present in the gas. This can be caused internally by a smaller number of already excited gas molecules, or externally by highly energetic cosmic rays entering the gas chamber. Then by applying a voltage, these electrons gain energy creating other electrons via ionising collisions. When more electrons are generated from the collisions than are lost, an avalanche is created, which causes the gas breakdown.

The breakdown voltage can be expressed by the following equation [6]:

$$V_B = \frac{Bpd}{\ln(Apd) - \ln[\ln(1 - \frac{1}{\gamma_{se}})]} \quad (2.1)$$

where  $V_B$  is the breakdown voltage,  $p$  is the pressure of the gas,  $d$  is the gap length,  $\gamma_{se}$  is the coefficient for secondary-electron emission (explained in section 2.1.2), and  $A$  and  $B$  are constants for a given gas that are determined experimentally.

However it is much easier to understand Paschen's law pictorially. Figure 2.1 illustrates the voltage breakdown curves for various gases. Each curve is slightly different, however all of them do exhibit a convex shape. Supposing if:

- **The gap length remains constant.** Starting with a large pressure, the mean free path of an electron within the gas is quite short, meaning it does not have sufficient time in between collisions for it to gain enough energy to cause an ionising collision with the neutral gas. As the pressure is then reduced, the mean free path increases, making it easier for the electrons to gain sufficient energy to undergo ionising collisions; until a

certain critical pressure that is (typically a  $pd$  of approximately 1 to 10 Torr cm). Beyond this, decreasing the pressure further causes the mean free path of the electron lengthen to a point that is comparable to the gap length, therefore this decreases the likelihood of an electron colliding with a neutral gas particle and the breakdown voltage increases.

- **The pressure remains constant.** When the gap length is very small, electrons are accelerated by a large electric field but are collected by the electrodes without undergoing collisions with the background gas. Increasing this gap length to a certain point gives the electrons the opportunity to collide with the background gas, producing ionising collisions. However, as the gap length continues to be increased, the strength of the electric field between the electrodes decreases, hence the electrons gain less energy between the collisions resulting in fewer ionising collisions with the background gas.

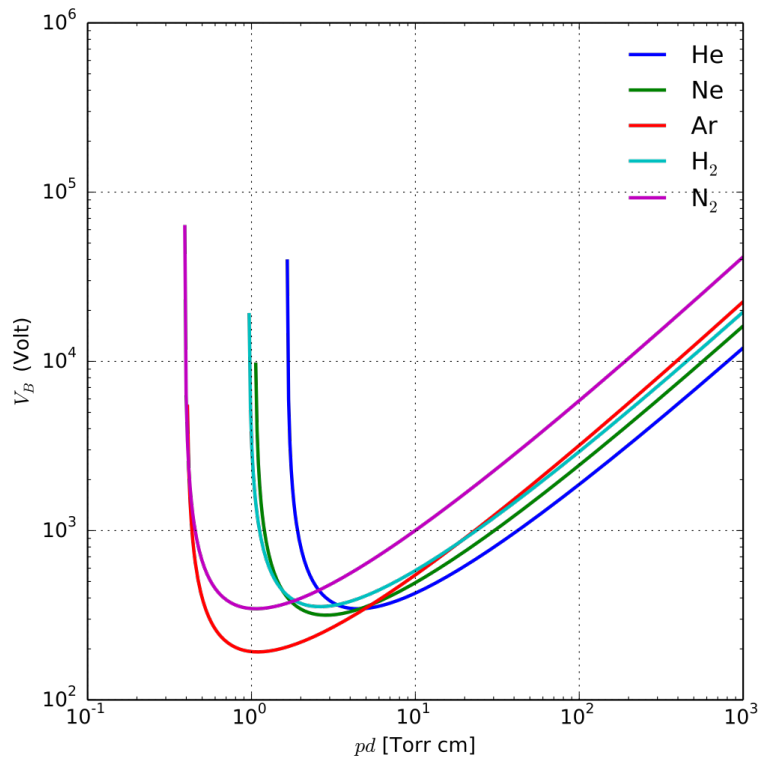


Figure 2.1: Paschen curve for Helium, Neon, Argon, Hydrogen, and Nitrogen gases [6].



### 2.1.2 DC Discharge

Consider a circuit as seen in figure 2.2. Two parallel electrodes with a DC voltage applied, and a neutral gas contained within a chamber. As the resistance of the variable resistor is decreased, which in turn increases the current through the plasma, one would observe three distinct discharge regions [7], observed in figure 2.3.

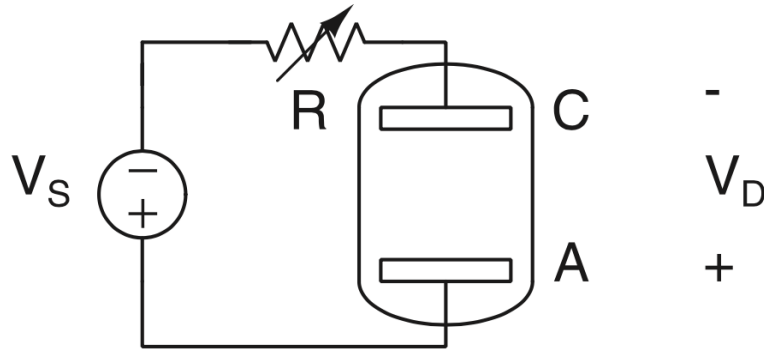


Figure 2.2: Circuit diagram with a source voltage ( $V_s$ ) and variable resistor ( $R$ ) to control the current through a discharge region (C to A) [7].

The first, is the dark discharge (or sometime referred to as the Townsend discharge) region. Initially, the voltage between the electrodes builds up as the only current through the plasma is caused by pre-existing electrons, say from cosmic radiation; however this current quickly saturates (seen from region A-B in figure 2.3). Then, once the electrons gain sufficient energy, they begin colliding with the background gas to produce additional electrons in a process called the *Townsend avalanche* (seen from region B-D in figure 2.3). Once this avalanche is self-sustaining, the voltage breakdown of the gas is reached (at point D in figure 2.3).

After the breakdown, the plasma is said to be in a glow discharge region. Here, the voltage across the plasma decreases since a transition from a gas to plasma state causes a decrease in resistance, implying that the ionisation process from the avalanche is more efficient (seen from region D-G in figure 2.3). This efficiency stems from the fact that the electrons are generated by a secondary means in addition to the standard Townsend avalanche. This process is called the secondary emission of electrons, which is caused the energetic collisions of ions and metastables with the surface of the cathode. These *secondary-electrons* are then accelerated by the electric field and cause further Townsend avalanches.

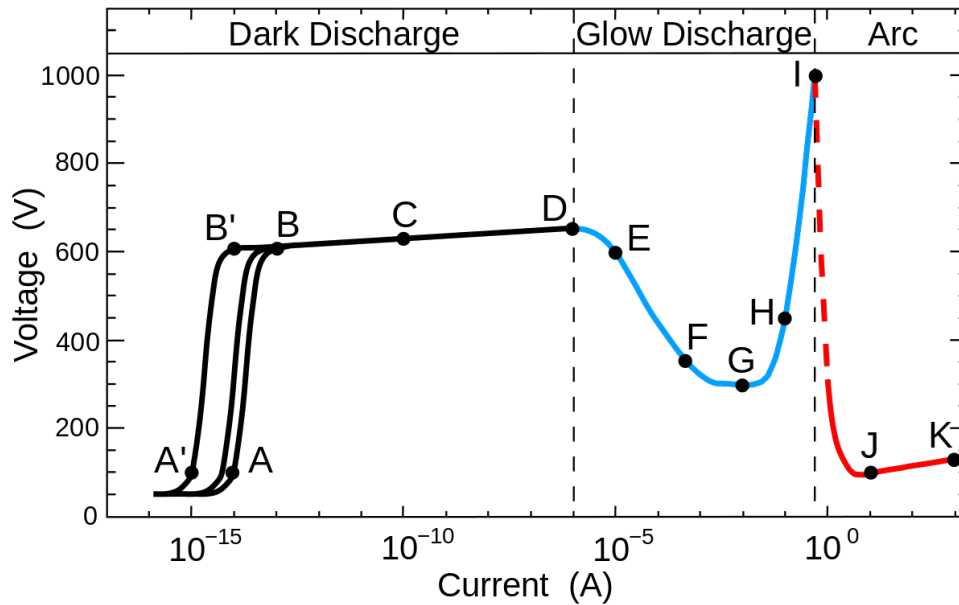


Figure 2.3: Depiction of the current-voltage relationship across three discharge regions [8].

At first, ion bombardment on the surface of the cathode is non-uniform but as the current generated from this increases, it eventually stabilises and the distribution of the plasma (and thus the ions) across the cathode become more uniform. This is referred to as *subnormal glow* and *normal glow* respectively. As the current is increased further, ion bombardment across the cathode becomes saturated as it covers the entire surface of the cathode (seen from region G-I in figure 2.3). This is referred to as *abnormal glow*, and increasing the current further causes the glow discharge to become an arc (at point I in figure 2.3).

In the arc discharge region, the ion bombardment onto the cathode causes the cathode to heat up to a point where electrons are generated via thermionic emission. This significantly reduces the resistance of the plasma, causing a very large drop of the voltage (seen from region I-J in figure 2.3).

For the purposes of this project, the arc discharge region will be avoided. The reason being, operating under arc conditions increases the electrode sputtering rate. *Sputtering* is the ejection of atoms from the electrode caused by the bombardment of energetic particles. While useful for processes such as ion etching [6], sputtering would not be favourable for the as the consumption of the electrode material is something to be avoided. Sputtering has the additional downside

of potentially contaminating the plasma composition as ejected atoms could end up reacting with the other plasma species.

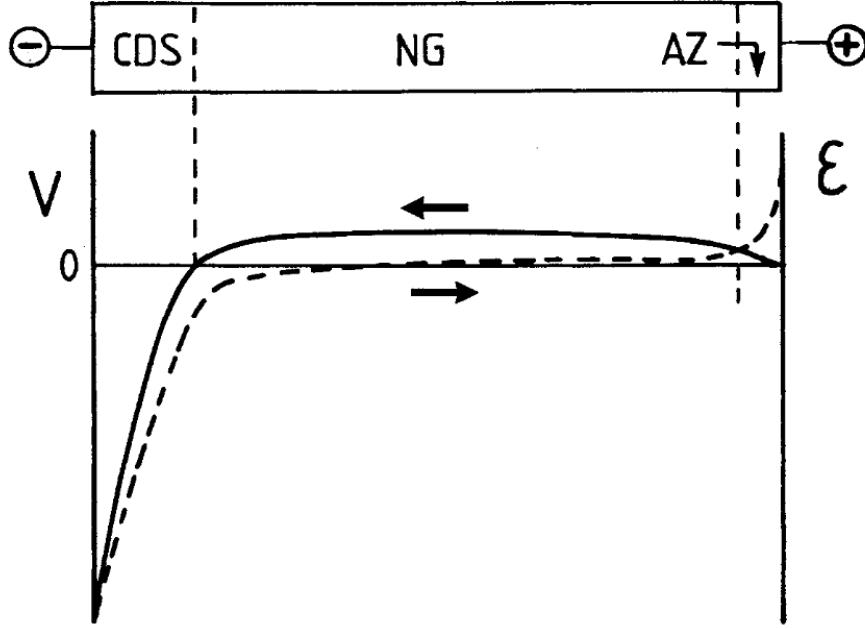


Figure 2.4: Schematic highlighting the regions present in a DC glow discharge [9]. The cathode is on the left and the grounded anode is on the right. (CDS is the cathode dark space, NG is the negative glow, and AZ is the anode dark space.

In a glow discharge there are typical three spatial regions present. These include a *cathode dark space*, a *negative glow* region, and the *anode dark space* [7, 9]. This can be observed in figure 2.4, that shows the potential in each region. Do note, as the distance between the electrodes is increased, additional regions may develop, however these three regions will always persist. The dark space regions are called *sheaths* while the negative glow region is known as the *bulk plasma*. Generally, the sheaths on the cathode will be much larger than that of the anode, as it corresponds to the region where electrons are being accelerated before gaining sufficient energy to cause ionising collisions. In contrast, the anode sheaths form to limit the electron current to the anode, maintaining current continuity over the discharge. Finally, the bulk plasma is the quasi-neutral region that contains the ions and electrons of the plasma.

### 2.1.3 AC Discharge

If the voltage source in the circuit of figure 2.2 were to be replaced with a low frequency AC source, the discharge behaviour would be almost identical to that of the DC discharge, with the caveat that the roles of the electrodes alternating between cathode and anode. This is provided that the half time period of an AC cycle is larger than the duration for ions and electrons to move across the electrodes [9].

However, as the frequency of the AC source is increased, typically to the region of radio or microwave frequencies, there is an asymmetry between the movement of the ions and electrons. The electrons are capable of responding to the change in the electric fields relatively quickly; however, due to the ions being significantly heavier than electrons, they have a much slower response time that is restricted by their inertia [10].

Since the ions cannot respond to the changing electric field quick enough, they respond to the time-averaged field thus are accelerated against both electrodes cross the sheath. On the other hand, the electrons begin accelerating through the bulk plasma towards the anode during the first half period of the AC signal. Then as the direction of the electric field reverses in the second half period of the signal, the positions of the anode and cathode flip, and any electron that has not collided with the original anode (which is now the cathode), gets accelerated through the bulk plasma towards the new anode. This oscillating behaviour confines the electrons, resulting in an increased likelihood of ionising collisions with the neutral background gas. As the frequency of the AC source is increased, more electrons become trapped in this regime, hence it is no surprise that the breakdown voltage of the plasma decreases [11]. This can be seen in figure 2.5

Astute readers may notice the minimal role of the secondary emission of electrons plays in the AC discharge. Because of the reduced of ion bombardments, there is less erosion on the electrodes, which increases its overall lifetime.

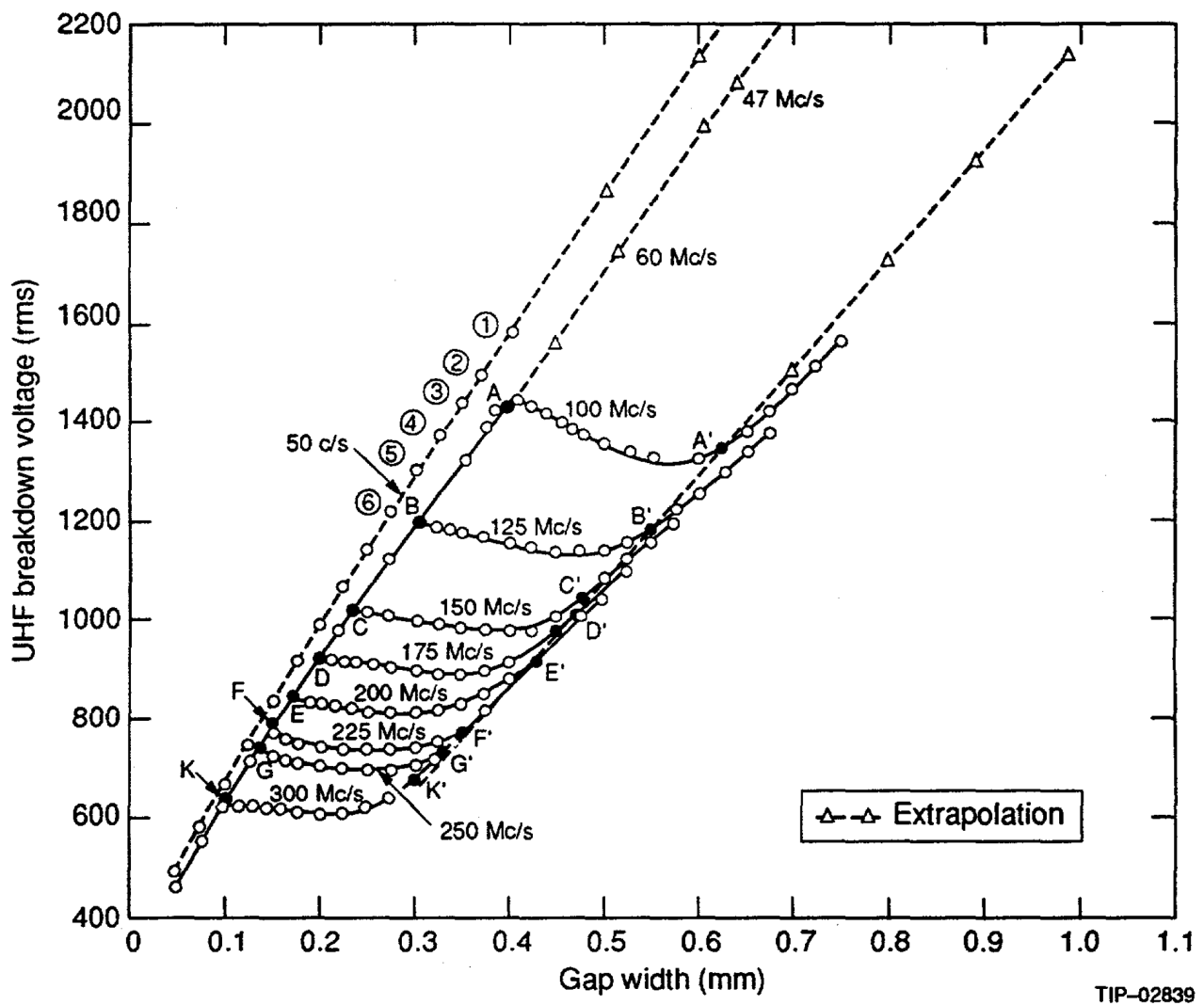


Figure 2.5: Paschen curve for AC discharge across various frequencies [12].

# Chapter 3

## Carbon Dioxide Splitting

### 3.1 Traditional Process

Before understanding the process of plasma-assisted CO<sub>2</sub> splitting, it would be useful to briefly explain the traditional thermally driven process. This process, sometimes referred to as pure CO<sub>2</sub> splitting, can take one of two possible forms. Often referred to as the reverse of coal burning, the overall reaction for CO<sub>2</sub> splitting can be written as:



This though is a simplification of the process, as it is most likely a two part mechanism [13]. The first half of the process would involve splitting the CO<sub>2</sub> into carbon monoxide (CO) and atomic oxygen (O) as seen in 3.2. The second step could take one of two possible pathways, however the most likely of the two would be the Boudouard reaction, seen in 3.3; however, this specific reaction is beyond the scope of this report.



Traditional thermal CO<sub>2</sub> splitting has not had much success to date, primarily due to the fact that CO<sub>2</sub> is an incredibly stable molecule with a Gibbs free energy of formation ( $\Delta G^\circ$ ) of -394 kJ mol<sup>-1</sup>. This is significantly higher than most other common gases as illustrated in figure 3.1.

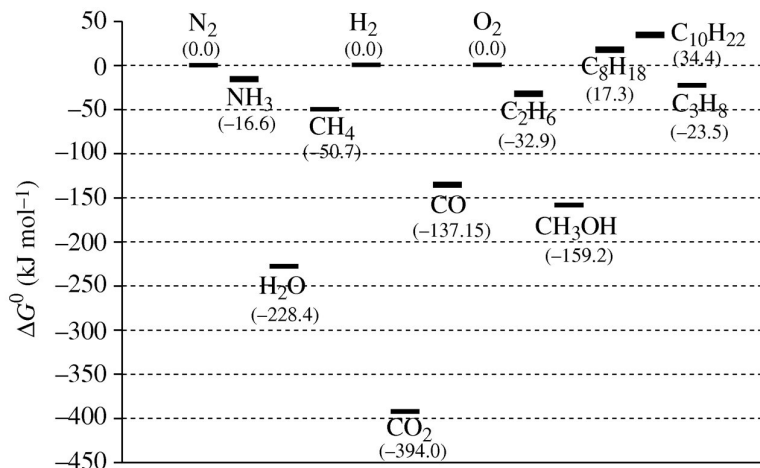


Figure 3.1: Gibbs free energy of formation for different chemicals based on data from the NIST database. [14]

The enthalpy of formation ( $\Delta H_f^\circ$ ) of the reaction in 3.2 is +283 kJ mol<sup>-1</sup>, meaning that it is endothermic. Thus in order to make this reaction favourable, high temperatures are required. Figure 3.2 highlights the conversion of such a reaction based on temperature, along with its corresponding energy efficiency [15]. This process could be improved by the presence of an active catalysts but this also increase the complexity and costs.

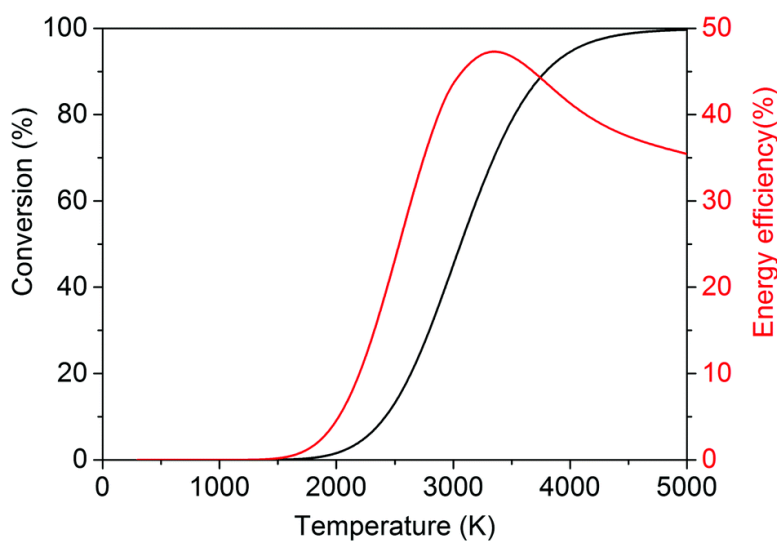
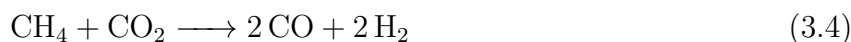


Figure 3.2: Thermal conversion and energy efficiency of CO<sub>2</sub> splitting as a function of temperature. [15]

Because of the low energy efficiency of pure CO<sub>2</sub> splitting, it is oftentimes more practical to include the use of a co-reactant. Ideally, this is done using a co-reactant with a higher Gibbs free energy (i.e. a less negative value) [14]. In the literature, the most common co-reactants for CO<sub>2</sub> splitting are methane (CH<sub>4</sub>,  $\Delta G^\circ = -50.7 \text{ kJ mol}^{-1}$ ) and hydrogen (H<sub>2</sub>,  $\Delta G^\circ = 0.0 \text{ kJ mol}^{-1}$ ).

The CO<sub>2</sub> splitting with CH<sub>4</sub> is a reaction that generates synthesis gas (syngas), principally used in the production of ammonia and methanol [1]. The process is referred as the dry reforming of methane and can be expressed as:



This reaction is also endothermic, with a  $\Delta H_f^\circ = +247 \text{ kJ mol}^{-1}$ , hence has to be run at high temperatures (between 1000 K to 1300 K, much lower than that of pure CO<sub>2</sub> splitting) and in the presence of a catalysts (typically nickel) [16]. However, the big limitation with this process is the formation of soot on the catalyst, reducing the yields.

As for using H<sub>2</sub> as a co-reactant to CO<sub>2</sub> splitting, this process is known as the Sabatier reaction. The reaction, seen in 3.5, is typically to generate synthetic natural gas but has other uses such as the production of water on the international space station [17].



The reaction is exothermic, with a  $\Delta H_f^\circ = -165.3 \text{ kJ mol}^{-1}$ , but does require a catalyst in order to achieve high conversion yields. Nonetheless, there are two issues with this process. The first being, unless water is the desired end product, a third of the H<sub>2</sub> used goes towards the creation of a waste product; not ideal when using this process at scale. The other issues has to do with the fact that most of the world's supply of H<sub>2</sub> comes from the process of steam reforming, which produces CO<sub>2</sub> as a by-product.



### 3.2 Plasma-assisted $\text{CO}_2$ Splitting

As highlighted above, there are several shortfalls with the traditional process of  $\text{CO}_2$  splitting. This is where the use of plasma, specifically non-thermal plasmas (i.e. generated by electric means), can be beneficial. In these plasmas, electrons have a higher temperature than the ions or the background gas. Energetic electrons in the plasma can dissociate molecules, even highly stable ones such as  $\text{CO}_2$  at standard temperatures and pressures [15].

Because of this behaviour, there is no need for heat and pressurised reactors, reducing the complexity (and thereby costs). This leads on to the second benefit, where the entire operation of such a reaction is described as a 'turn-key' process due to the ability to instantly turn the plasma on and off, with minimal stabilisation times. There is also no need for rare earth metals to be used as catalysts, and it has been shown that plasma reactors can have good scalability as shown by Kogelschatz in [18].

There are several different methods to generate plasma for  $\text{CO}_2$  splitting in the literature, however the most common are: dielectric barrier discharges, gliding arc discharges, and radio frequency(RF)/microwave discharges. This report will only cover the RF/microwave discharges as it is the process being used, with several examples in the literature highlighted below.

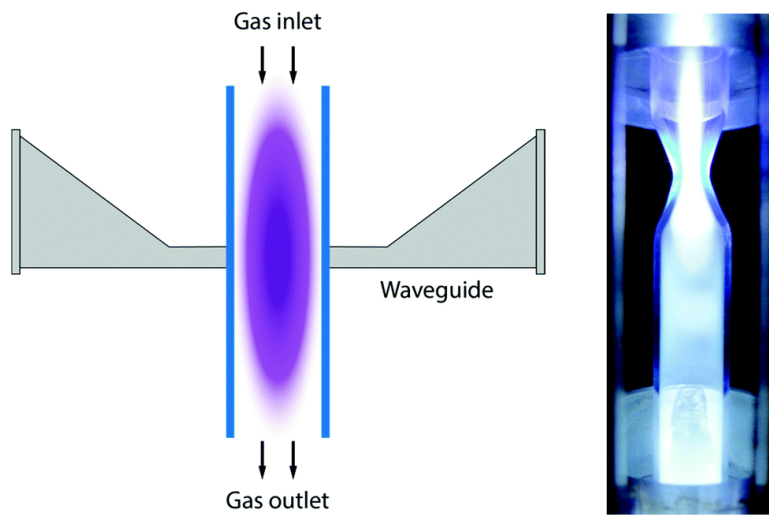


Figure 3.3: Schematic of microwave reactors for  $\text{CO}_2$  splitting. [15]

Many experiments utilise a structure as seen in figure 3.3, whereby the gas is fed in via a quartz tube coupled with an external wave guide where the microwave discharge is generated. Such

a design was used by Spencer and Gallimore [19] to achieve a conversion efficiency of approximately 90%; although this came at the cost of energy efficiency which reached a maximum of 3%. The authors went on to state that such a system would not be suitable for CO<sub>2</sub> emission reductions.

Nonetheless, other designs for RF/microwave discharges exist such as the one developed by Xu et al [20]. Their design utilised a co-reactant called *trans*-stilbene. Unlike the co-reactants previously mentioned, which were gaseous, *trans*-stilbene is a liquid. Because of this, the plasma had to directly contact the solution, which was achieved via a plasma jet reactor. The jet nozzle had to be placed 4 mm above the surface of the liquid, and the final product of this reaction was CO and epoxides (a popular compound used for detergents, adhesives, and plastics). The authors were able to obtain a 75% yield on epoxides and a splitting of approximately 70% of the CO<sub>2</sub> in the plasma. As such, this will be the process that is emulated in this report.

# Chapter 4

## Split Ring Resonator

In order to generate a plasma jet, a device known as a *split ring resonator* (SSR) was used. An illustration of this device can be seen in figure 4.1. The design of a SSR is quite simple, consisting of a conducting ring, usually made of copper, laid on top of a dielectric substrate. The bottom of the dielectric consist of a ground plane that covers the entirety of the surface. This has the added benefit of dispersing the heat generated from the SSR. As seen in figure 4.1, there is a small gap made on the top surface that breaks the copper ring, which is where the plasma discharge occurs.

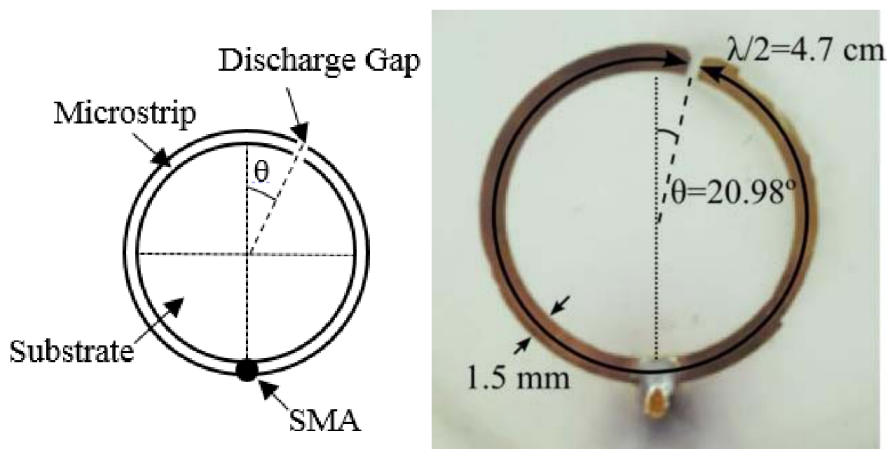


Figure 4.1: Schematic (left) and photo (right) of SSR [21].

## 4.1 Overview

In order to achieve a discharge, an *ultra high frequency* (UHF) voltage is applied to the SSR via the SMA connector. The exact frequency to be used is governed by two factors: the mean circumference (which is measured from the middle) of the top conducting ring and the dielectric constant of the substrate used. The mean circumference is usually designed to be half the wavelength corresponding to the desired frequency. The dielectric constant is required to determine the speed of light in the dielectric medium used. Thus, an equation for the frequency used for a given SSR is:

$$f = \frac{c}{\lambda\sqrt{\varepsilon_r}} \quad (4.1)$$

The reason why the mean circumference is designed to be half the desired wavelength is due to power efficiency. Due to this design, the ends of the SSR (i.e. where the gap is) will be 180° out of phase from each other. Because of this, when one end of the SRR is at the peak of the AC cycle, the other will be at a trough; thus the potential difference between the two ends has been doubled. This geometric trick allows for the doubling of the strength of the electric field at a constant power.

Astute readers may notice another peculiarity with the SSR seen in figure 4.1, in that it is not symmetrical. Instead, the discharge gap appears to be offset towards one side of the device. This is deliberate as the offset gap allows for the impedance matching of the SRR to the impedance of the power supply used, thus maximising the power transfer. This offset angle is measured from the very centre of the ring, and is determined using the expression:

$$\theta = \arccos\left(1 - \frac{Z_{in}\pi}{Z_0Q}\right) \quad (4.2)$$

where  $Z_{in}$  is the input impedance of the power supply,  $Q$  is the quality factor, and  $Z_0$  is the characteristic impedance of the SRR. Typically, the input impedance of many power supplies is 50 Ω. The characteristic impedance can be determined by the width of the top copper trace,

the thickness of the dielectric substrate, and the dielectric constant of the substrate. As for the quality factor, this parameter is given on the data sheet of the substrate used.

## 4.2 Production

The SSR device needed for this project requires a slight modification to the design compared to the traditional SSR. In order to create a small jet of plasma, through holes are needed at the region of the gap of the SSR. This would allow the gases to react with the plasma, then pass through the hole.

However, to determine if this small change had any significant effects on the behaviour of the SSR, simulations were run to better understand what was going on. Specifically, *Particle-in-cell* (PIC) simulations were used; and the software used is called *XOOPIC*. Further information on PIC simulations and XOOPIC can be found in the appendices.

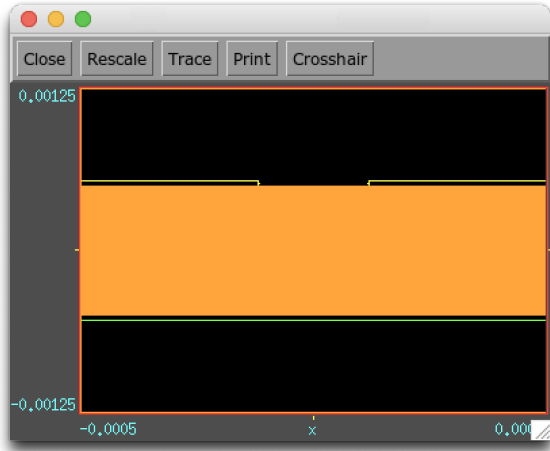
### 4.2.1 Simulations

Multiple different simulations were run to understand the characteristics of the plasma, however they could be broadly broken down into three groups. For all these simulations, a cross sectional plane of the discharge gap of the SSR was modelled. The reasoning for this was that the plasma formed would typically be constrained around the gap. Though the ring of the SSR is a circle, the discharge gap is small relative to the overall device, hence can be approximated to be a rectangle. Thus such a simulation would be valid assuming that the electric field across the gap is constant along all points of the ring. For all the following simulations, the parameters can be found in table 4.1 unless specified otherwise.

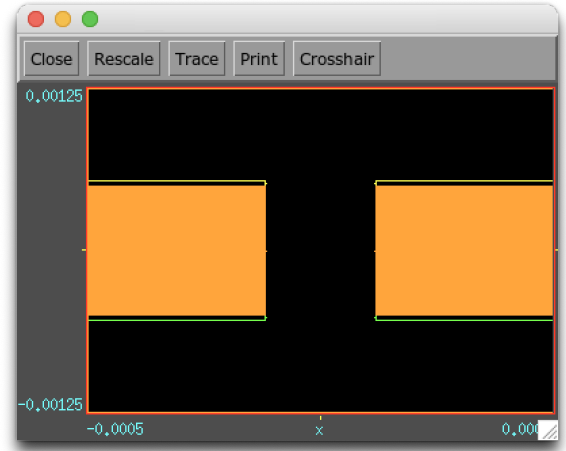
The first of these simulation groups was to simply study the effects of introducing a through hole to the SSR. For this test, all simulation parameters were kept identical, the only difference would be the introduction design of the gap. An visualisation of the simulations could be seen in the figure below. In figure 4.2a, the dielectric substrate (seen in gold) and the bottom

Table 4.1: Simulation parameters of SSR in XOOPIC.

Parameters	Value	Units
Domain x-axis	1.0	mm
Domain y-axis	2.5	mm
Dielectric thickness	500	$\mu\text{m}$
Dielectric constant	3.66	
Equipotential thickness	40	$\mu\text{m}$
Gas pressure	780	Torr
Gas temperature	25	meV
Potential Difference	150	V
Frequency	1	GHz
Time step	0.1	ps



(a) Cross section of SSR without hole in gap.

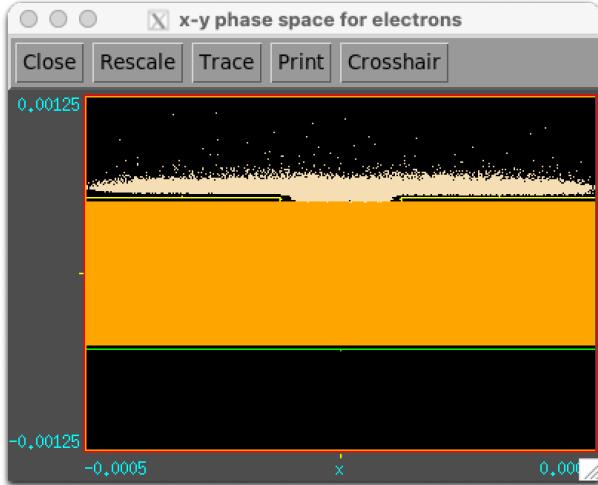


(b) Cross section of SSR with hole in gap.

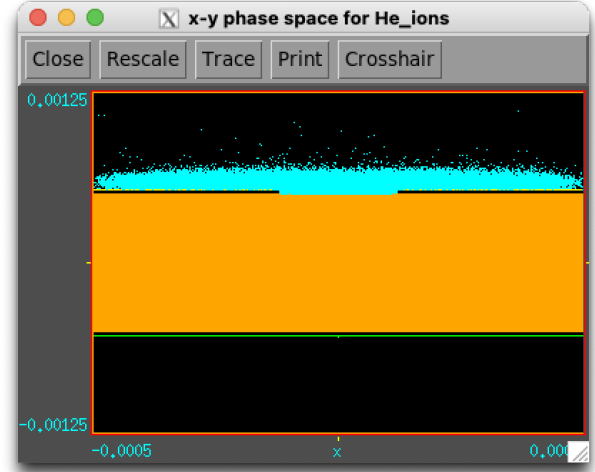
Figure 4.2: A comparison of SSR with and without hole in gap.

electrode (seen in green) is kept intact as a single structure, whereas the top electrode (seen in yellow) is split. However in 4.2, all three layers of the SSR are split into two. The size of the discharge gap chosen was  $240 \mu\text{m}$ , the dielectric constant of the substrate was 3.66, and the voltage used was 150 V at 1 GHz.

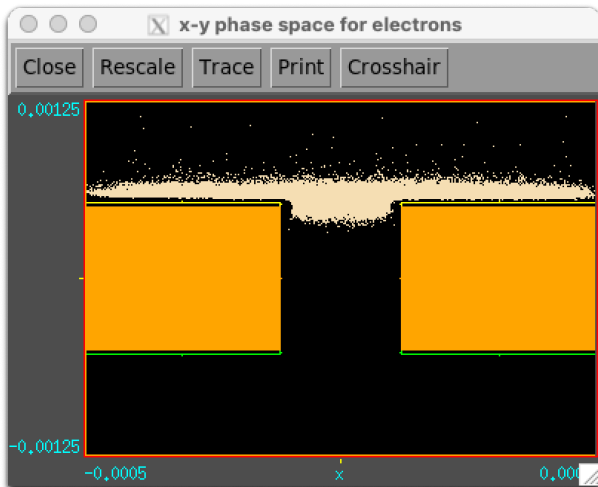
The results of the simulation after it stabilised can be seen in figure 4.3. The immediate difference that can be observed is the fact that the ions and electrons, represented as blue and orange dots respectively, tended to ‘sit’ deeper into the gap in the case with the through hole. Intuitively, this would make sense as these particles are not colliding with the substrate (which in XOOPIC meant that they were removed from the simulation domain). Additionally, it was hypothesised that strength of the electric field between the top electrodes and the ground plane could potentially play an effect in how deep the ions and electrons ‘sit’ in the gap of the SSR.



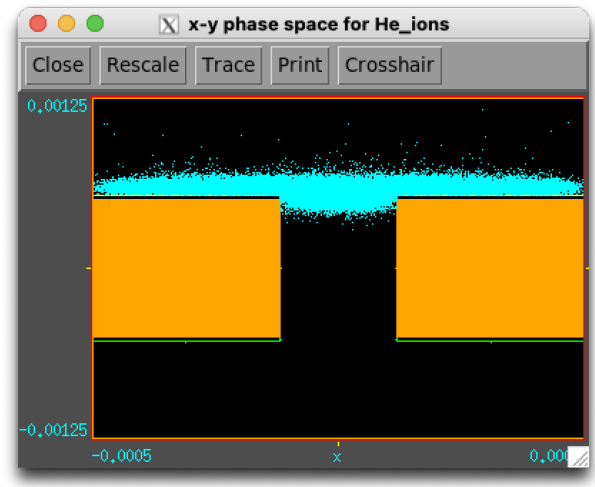
(a) Plot of electrons in SSR without hole in gap.



(b) Plot of ions in SSR without hole in gap.



(c) Plot of electrons in SSR with hole in gap.



(d) Plot of ions in SSR with hole in gap.

Figure 4.3: Comparison of SSR with and without hole in gap.

This leads into the second group of simulations that were run, where the separation distance between the top and bottom electrodes were investigated, which also had the added benefit of identifying if the ideal dielectric substrate thickness to be used when manufacturing the SSR. The parameters used for the size of the gap, the dielectric constant of the substrate, and the potential difference were kept the same as the first group. As for the dielectric thickness, simulations were run with values of 0.2 mm, 0.5 mm, 1.0 mm, 1.5 mm, and 2.0 mm.

From the cross sectional view of the density plot of electrons in figure 4.5, all simulations performed quite similarly. The electrons seem to extend through the gap by roughly the same distance. However, even though the dielectric thickness did not play a large role in the plasma, it would be preferable to choose a thicker dielectric for the sturdiness of the board.

The final group of simulations run were to establish the effect of the discharge gap widths. The sizes used were a gap width of 120  $\mu\text{m}$ , 240  $\mu\text{m}$ , 360  $\mu\text{m}$ , and 480  $\mu\text{m}$ .

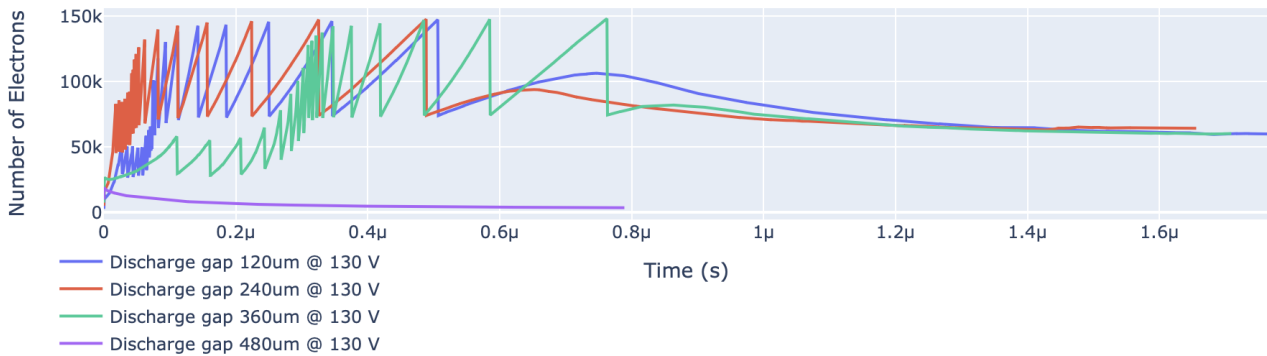
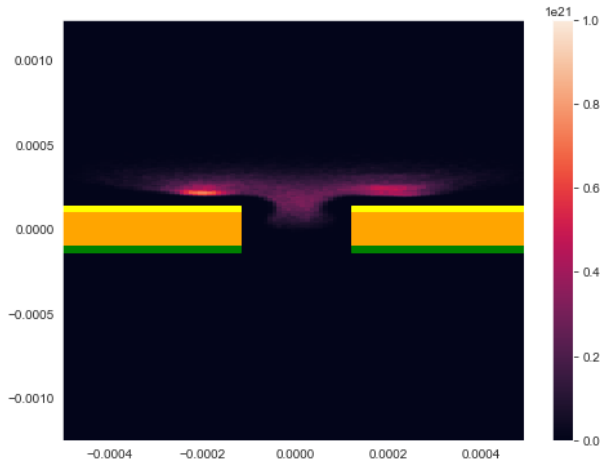


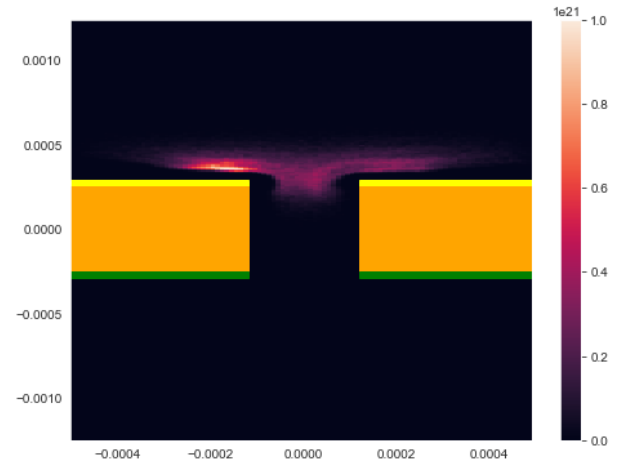
Figure 4.4: Time series plot of number of electrons across different discharge gaps.

The results of these simulations can be seen in figure 4.4. From these tests, only three simulations were successful as the run with a gap width of 480  $\mu\text{m}$  lost all the seed electrons. The most likely explanation for this behaviour was that the voltage used (150 V) was not sufficient to ignite a discharge. As for the other three runs, the big difference seemed to be the initial growth rate. A gap width of 240  $\mu\text{m}$  appeared to be the optimum. One would expect that the smallest gap width would perform the best, however as seen by Paschen's law (refer to Chapter 2.1.1), reducing the distance between electrodes too much would cause the electrons to be simply lost to the electrode. This could possibly explain why the run with a gap width of 120  $\mu\text{m}$  underperformed.

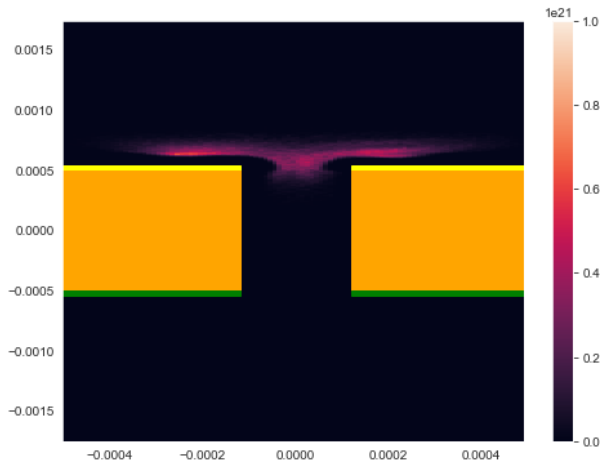




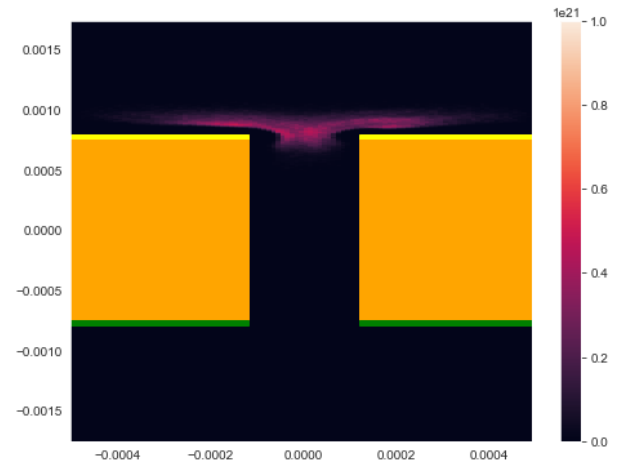
(a) Dielectric thickness of 0.2 mm.



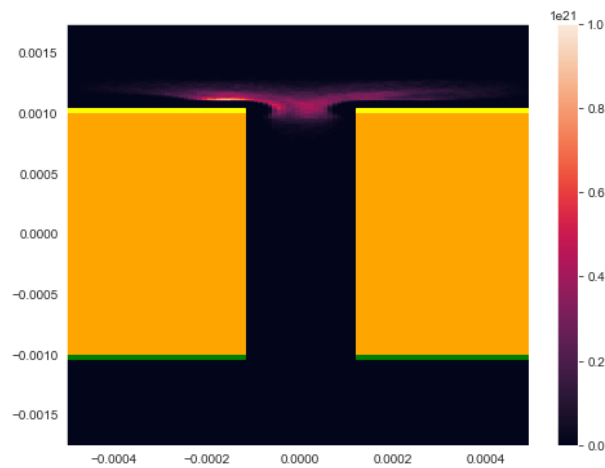
(b) Dielectric thickness of 0.5 mm.



(c) Dielectric thickness of 1.0 mm.



(d) Dielectric thickness of 1.5 mm.



(e) Dielectric thickness of 2.0 mm.

Figure 4.5: Comparison of dielectric thickness on SSR with hole in gap.

### 4.2.2 Design

Armed with this information, a design of the SSR to be used was made. The first step was to select the PCB substrate to be used, as its dielectric constant is a central parameter for all other calculations of the SSR. The material selected was the RO4350B<sup>TM</sup> material from Rogers corporation. This specific material was chosen as it is designed for high power UHF designs, and its relatively low fabrication costs. Additionally, the RO4350B<sup>TM</sup> material did not require any special treatments or procedures to produce a through hole. According to its data sheet, the RO4350B<sup>TM</sup> board has a dielectric constant of 3.66, and a dissipation factor of 0.0031 (which can be converted to the quality factor).

The next step was to determine the resonant frequency for the SSR. Ideally, a higher resonant frequency would improve the quality factor, reducing power losses and making it more likely that a plasma discharge occurs. However, a frequency that was too high would increase power requirements and would also reduce the size of the SSR. Therefore, a compromise between the two needed to be struck, and a target frequency 950 MHz was chosen.

Feeding this number into equation 4.1, the corresponding wavelength was 0.165 m. Since the circumference of the SSR is given as  $\lambda/2$ , this meant that the design had a circumference of 8.25 cm; which was a radius of approximately 1.3 cm.

The next step was to determine the characteristic impedance. Conventionally, this impedance should be close to the value of the input impedance, which for power supply used was 50  $\Omega$ . As mentioned earlier in this chapter, three factors dictate the value of this parameter. The dielectric constant of the substrate was 3.66, a fixed value based on the material used. As stated in the previous section, a thicker dielectric substrate would be preferable. The RO4350B<sup>TM</sup> material came in a thickness of 0.5 mm, 0.8 mm, and 1.55 mm; with the costs increasing with thickness. Thus, as compromise between the structural rigidity PCB and cost, a thickness of 0.8 mm was selected. By using the equations by Wheeler in [22], a trace width of approximately 1.7 mm would produce a characteristic impedance of 50.1  $\Omega$ .

Finally using equation 4.2, the offset angle of the SSR was calculated. As from the datasheet,

the dissipation factor of the RO4350B<sup>TM</sup> material is 0.0031. The reciprocal of this value was taken to determine the quality factor, which was 323. This would give a gap with an offset angle of 7.99. Again based on the simulations above, the ideal gap width was 240  $\mu\text{m}$ , however the minimum size drill hole size would limiting factor when manufacturing, hence the gap width was slightly increased to 250  $\mu\text{m}$ .

With these parameters known, the next stage was to create the PCB design. This was done using the open-sourced PCB design software called *KiCad*. An illustration of the final design can be seen in figure 4.6. As seen from the figure, four SSR designs were made. These were done to test various gap designs that could not be replicated using XOOPIC simulations. These designs could be broken down into two categories: single versus multiple drill hole in SSR gap; and the presence versus absence of ‘finger-like’ copper pours next to the SSR gap. The permutations of these categories resulted in the four designs, with a close up image of each seen in figure 4.7. All four designs also used an SMA connector as the input source.

## 4.3 Testing

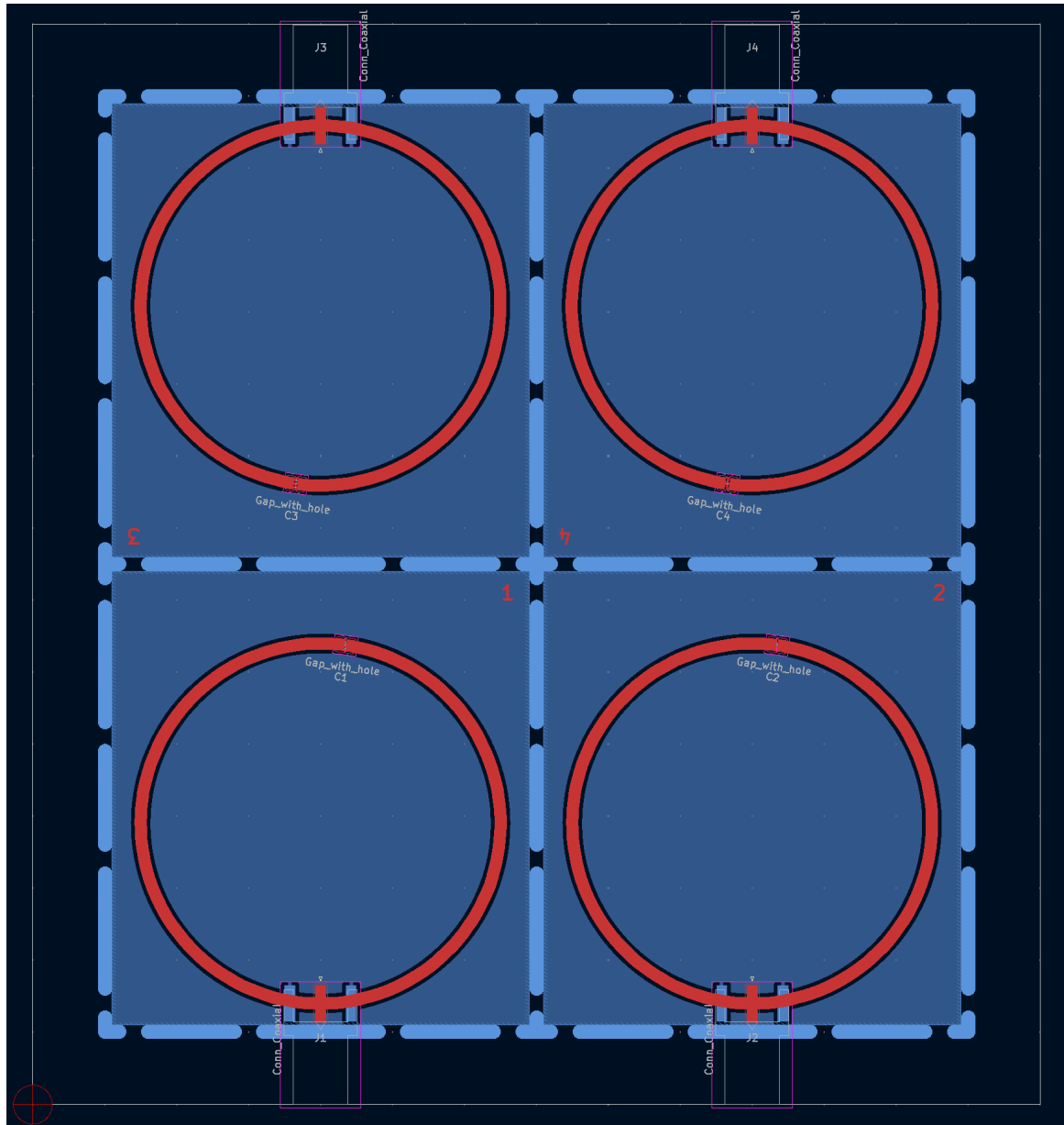
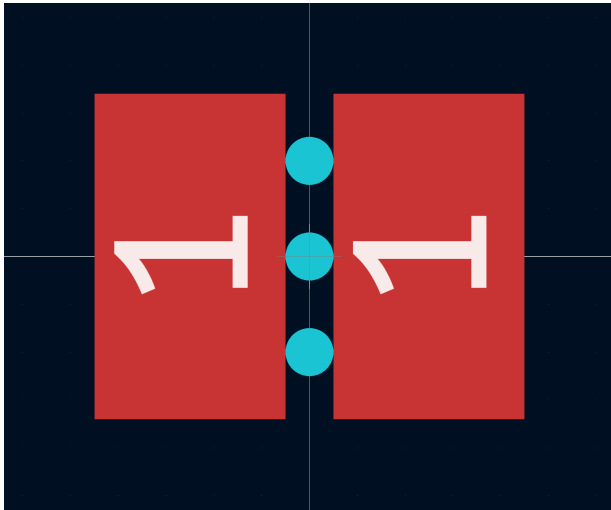
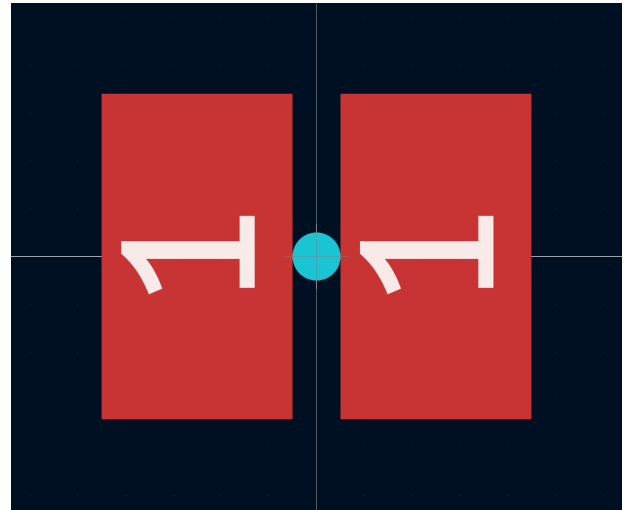


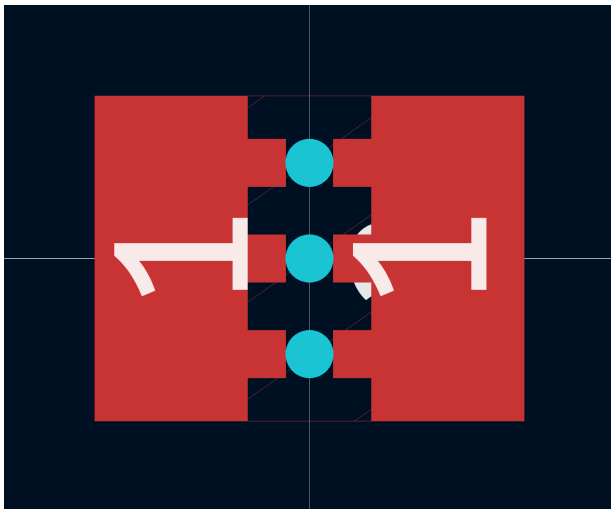
Figure 4.6: PCB design of SSR in KiCad.



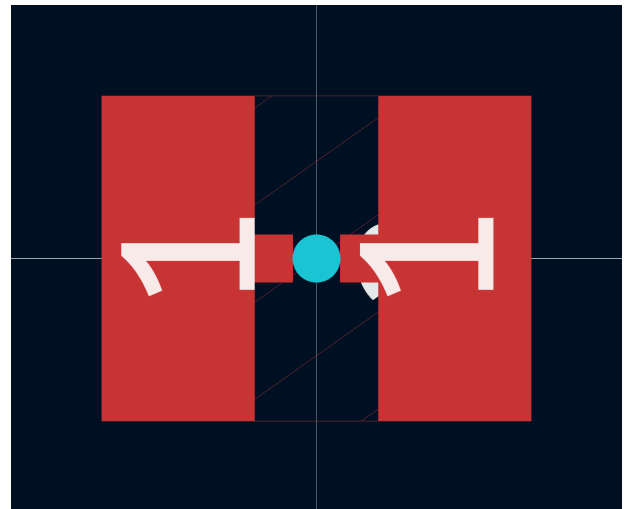
(a) Design 1 - Multiple holes, no 'fingers'.



(b) Design 2 - Single hole, no 'fingers'.



(c) Design 3 - Multiple holes, with 'fingers'.



(d) Design 4 - Single hole, with 'fingers'.

Figure 4.7: Close up of SSR gap designs.

## Chapter 5

# Epoxidation Process

## Chapter 6

### Gas recirculation

## Chapter 7

## Conclusion



# Appendix A

## Particle-in-Cell Simulations

Plasmas are complex non-linear systems and contain many unknown variables. Therefore, simplified models are often used to capture major physics of the system whilst ignoring details that can be considered negligible. There are several types of plasma models but the most commonly used methods are fluid description models and kinetic description models [23].

The fluid description method aims to generalise the plasma quantities, such as its density and velocity, by averaging them over a 2D or 3D region. This is achieved by numerically solving the fluid equations; obtained by utilising the velocity components of the Boltzmann equation [23]. Then, the electromagnetic fields are obtained by combining the fluid equations with Maxwell's equations.

In contrast, kinetic description models track the position and velocities of particles within the plasma, taking into account the electromagnetic forces acting on them. As a general rule of thumb, fluid models simulate the plasma behaviour over a macroscopic scale; whilst kinetic models highlight plasma behaviour at the microscopic level.

Particle-in-cell (PIC) simulations are a variant of kinetic description models that tend to be favoured because of its easy formulation. Real-world plasma systems contain a prodigious number of particles, which include electrons, ions, and the background neutral gas; thus, tracking all these particles would be immensely computationally taxing. PIC simulations partially solve

this by tracking so-called *super-particles* [24]. Each super-particle is scaled to represent a number of “real” particles. This scaling factor does not affect the trajectory of the super-particles as the motion of particles within a electromagnetic field are only governed by its mass to charge ratio (see the Newton-Lorentz expression in equation A.3) [24]. For the rest of this chapter, the term super-particle and particles are used interchangeably.

The PIC simulations discussed in this report are known as 2D-3v simulations, i.e. they are 2-dimensional in space but 3-dimensional in velocity. In these simulations, the particle properties (i.e. their position and velocity) are defined in continuous space within the simulation domain. However, the electromagnetic field values are only specified at fixed grid points. Therefore, intermediary steps are required to discretise charges and current densities onto the grid and also interpolation of forces by fields on the particles. These particles and fields are updated sequentially, with time being advanced in small discrete constant steps. An overview of this procedure can be seen in figure A.1 [25]. The rest of this chapter is dedicated to providing an overview of each process in the flow chart.

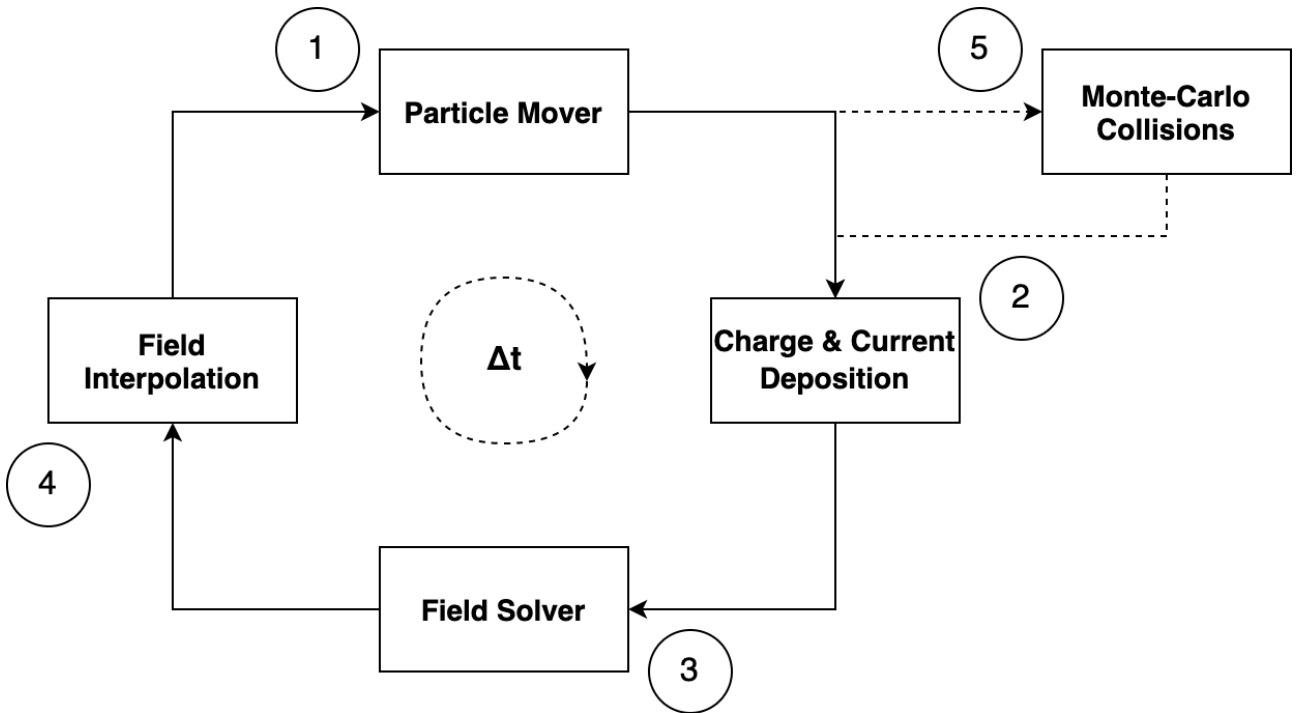


Figure A.1: Process flow of PIC simulations.

## A.1 Particle Mover

When first launching the PIC simulation, a random distribution of particle positions and velocities is initialised within the simulation domain. The acceleration of a particle is given by Newton's second law:

$$\frac{d\mathbf{v}}{dt} = \frac{\mathbf{F}}{m} \quad (\text{A.1})$$

The force acting on the particle is determined by the Lorentz force:

$$\mathbf{F} = q(\mathbf{E} + \mathbf{v} \times \mathbf{B}) \quad (\text{A.2})$$

where  $\mathbf{E}$  and  $\mathbf{B}$  are the electric and magnetic fields respectively, and  $q$  corresponds to the charge of the particle.

Combining equations A.1 and A.2 gives the Newton-Lorentz equation:

$$\frac{d\mathbf{v}}{dt} = \frac{q}{m}(\mathbf{E} + \mathbf{v} \times \mathbf{B}) \quad (\text{A.3})$$

As for the particles velocity, it is given by:

$$\frac{d\mathbf{s}}{dt} = \mathbf{v} \quad (\text{A.4})$$

In order to obtain the particle velocity and position, equations A.3 and A.4 have to be numerically integrated with respect to time using the *finite-difference method*; specifically the *leapfrog method* [26]. Thus, the new finite-difference forms of the respective equations are:

$$\frac{\mathbf{v}^{t+\frac{1}{2}} - \mathbf{v}^{t-\frac{1}{2}}}{dt} = \frac{q}{m}(\mathbf{E} + (\frac{\mathbf{v}^{t+\frac{1}{2}} + \mathbf{v}^{t-\frac{1}{2}}}{2}) \times \mathbf{B}) \quad (\text{A.5})$$

$$\frac{\mathbf{s}^{t+1} - \mathbf{s}^t}{dt} = \mathbf{v}^{t+\frac{1}{2}} \quad (\text{A.6})$$

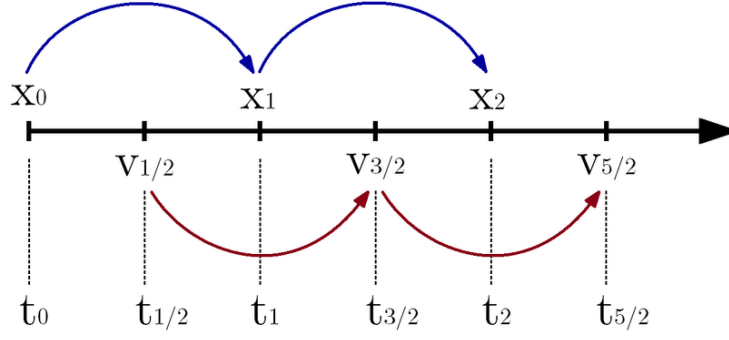


Figure A.2: Illustration of forward-difference and central-difference form [27].

Notice that the particle position is given by the *forward-difference form*, whereas its velocity is given by the *central-difference form*. This is done to conserve the energy of the dynamic system. An intuitive explanation for this is that when solving for the updated position of the particle, its average velocity should be used. Using either the initial or final velocities can result in the particle gaining energy if its accelerating, or losing energy if its decelerating. A visualisation of the difference can be seen in figure A.2.

To solve the Newton-Lorentz equation, the de-facto method used is the *Boris algorithm* [28] for its accuracy, speed, and simplicity. The method first redefines both velocity terms as:

$$\mathbf{v}^{t-\frac{1}{2}} = \mathbf{v}^- - \frac{q\mathbf{E}}{m} \frac{dt}{2} \quad (\text{A.7})$$

$$\mathbf{v}^{t+\frac{1}{2}} = \mathbf{v}^+ + \frac{q\mathbf{E}}{m} \frac{dt}{2} \quad (\text{A.8})$$

When substituted back into the the finite-difference Newton-Lorentz equation (equation A.5), this eliminates the electric field, resulting in an equation that expresses the rotation of the particle's velocity:

$$\frac{\mathbf{v}^+ - \mathbf{v}^-}{\Delta t} = \frac{q}{2m}(\mathbf{v}^+ + \mathbf{v}^-) \times \mathbf{B} \quad (\text{A.9})$$

Because it describes a rotation, it can be solved geometrically. Using the following 2D case seen in figure A.3, it can be determined that the angle through which the velocity rotates is:

$$\tan\left(\frac{\theta}{2}\right) = \frac{\mathbf{v}^+ - \mathbf{v}^-}{\mathbf{v}^+ + \mathbf{v}^-} = \frac{q\mathbf{B}}{m} \frac{\Delta t}{2} \quad (\text{A.10})$$

This angle can also be represented in vector form, referred to as  $\mathbf{T}$ . Using this vector form, a bisecting vector  $\mathbf{v}'$  can be obtained is parallel to the  $\mathbf{v}^+ + \mathbf{v}^-$  vector (the sum of the pre-rotation and post-rotation vector), and perpendicular to both the  $\mathbf{T}$  vector (the scaled magnetic field) and the  $\mathbf{v}^+ - \mathbf{v}^-$  vector (the difference between the post-rotational and pre-rotational velocity).

$$\mathbf{v}' = \mathbf{v}^- + \mathbf{v}^- \times \mathbf{T} \quad (\text{A.11})$$

Finally to obtain the  $\mathbf{v}^+ - \mathbf{v}^-$  vector, this intermediate vector  $\mathbf{v}'$  is combined with a new vector  $\mathbf{S}$  which can be thought of as a scaled version of vector  $\mathbf{T}$  seen in equation A.13.

$$\mathbf{v}^+ = \mathbf{v}^- + \mathbf{v}' \times \mathbf{S} \quad (\text{A.12})$$

$$\mathbf{S} = \frac{2\mathbf{T}}{1 + \mathbf{T}^2} \quad (\text{A.13})$$

Thus, in order to determine the new velocity of the particle:

1. First calculate the velocity of the particle over the first half time step using equation A.7.

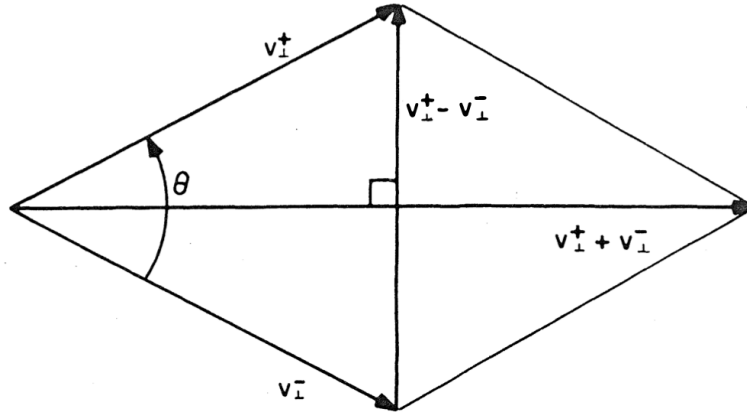


Figure A.3: Visualisation of velocity rotation from the Boris algorithm [28].

2. Then perform the full rotation of the velocity due to the magnetic field using equations A.11 and A.12.
3. Finally, calculate the velocity of the particle over the second half time step using equation A.8.

To obtain the particles new position, substitute the newly calculated velocity of the particle into equation A.6. Once calculated, the positions of each particle in the simulation can be updated.

## A.2 Charge and Current Deposition

Once the particles have been moved, their charge and current densities are discretised onto a the specified grid. The exact method of discretising these properties depends on the type of grid for the PIC simulation. The one described in this report is for a uniform 2D rectilinear grid, known as *bilinear interpolation* [29].

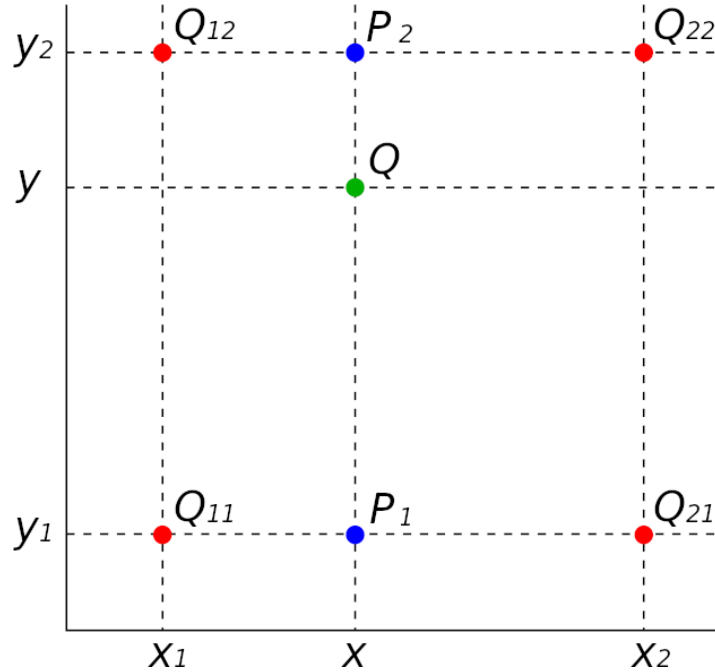


Figure A.4: Interpolation from the grid to the particles [30].

Consider the following case in figure A.4. The charge of the particle within the grid cell is distributed across the four vertices of the cell, called the *nodes*. The total charge experienced

by each node must equal to the charge of the particle, with nodes closest to the particle experiencing the greatest weight. This can be expressed as:

$$\begin{aligned}
 Q_{11} &= Q \frac{(x_2 - x)(y_2 - y)}{(x_2 - x_1)(y_2 - y_1)} \\
 Q_{12} &= Q \frac{(x_2 - x)(y - y_1)}{(x_2 - x_1)(y_2 - y_1)} \\
 Q_{21} &= Q \frac{(x - x_1)(y_2 - y)}{(x_2 - x_1)(y_2 - y_1)} \\
 Q_{22} &= Q \frac{(x - x_1)(y - y_1)}{(x_2 - x_1)(y_2 - y_1)}
 \end{aligned} \tag{A.14}$$

Intuitively, the weight of a node corresponds to the ratio of the area of the rectangle opposite (formed by the point of the particle and the point of the opposite node) and the total area of the cell.

Once the (weighted) charges at each node point has been calculated for all particles, the charge density of a node can be determined by summing the total charge on the node from all particles, then dividing by the area of the cell. This node area is typically given as  $(x_2 - x_1)(y_2 - y_1)$ , with the exception being nodes at the edges or corners of the simulation domain. With such cases, the resulting area is halved and quartered respectively.

A similar process is done to determine the current densities around a node. However, rather than just summing the charges, the total sum of the product between the particles charge and average velocity are taken.

## A.3 Field Solver

The field solver utilises the charge and current densities at the grid points to determine their corresponding electric and magnetic field values by solving Maxwell's equations. This report will only consider the electrostatic case and therefore will focus on the process of computing the electric field values.

Gauss's law dictates that the divergence of the electric field in a region is proportional to its

charge density:

$$\nabla E = \frac{\rho}{\varepsilon_0} \quad (\text{A.15})$$

The electric field is determined as the gradient of the electric potential, and by substituting that into the above equation results in Poisson's equation:

$$-\nabla^2 \phi = \frac{\rho}{\varepsilon_0} \quad (\text{A.16})$$

Considering a 2D case with a cartesian coordinate system, Poisson's equation can be rewritten as:

$$\frac{\partial^2 \phi}{\partial x^2} + \frac{\partial^2 \phi}{\partial y^2} = -\frac{\rho}{\varepsilon_0} \quad (\text{A.17})$$

In order to solve Poisson's equation in a discretised domain, the finite-difference method is employed. Specifically using the central-difference, the resulting approximation seen in equation A.18 is produced, which is classed as second order accurate.

$$\frac{\phi_{x+\Delta x, y} - 2\phi_{x, y} + \phi_{x-\Delta x, y}}{\Delta x^2} + \frac{\phi_{x, y+\Delta y} - 2\phi_{x, y} + \phi_{x, y-\Delta y}}{\Delta y^2} = -\frac{\rho}{\varepsilon_0} \quad (\text{A.18})$$

There are several method to solve such an equation numerically. An overview of method used by XOOPIC (simulation program used in this work, see chapter 4) is described below.

The Poisson equation is classed as an elliptic partial differential equation, which can be written in this form [31]:

$$\mathcal{L}u = \lambda \quad (\text{A.19})$$

where  $\mathcal{L}$  is the elliptical operator and  $\lambda$  is the source term.



It is then possible to rewrite this as a diffusion equation (i.e. with respect to time):

$$\frac{\partial u}{\partial t} = \frac{\partial^2 u}{\partial x^2} + \frac{\partial^2 u}{\partial y^2} - \lambda \quad (\text{A.20})$$

which is equivalent since as  $t \rightarrow \infty$ ,  $\frac{\partial u}{\partial t} \rightarrow 0$ .

Therefore, equation A.20 can be expressed as a diffusion equation in the finite-difference form:

$$\frac{\phi_{x,y}^{t+\Delta t} - \phi_{x,y}^t}{\Delta t} = \frac{\phi_{x+\Delta x,y} - 2\phi_{x,y} + \phi_{x-\Delta x,y}}{\Delta x^2} + \frac{\phi_{x,y+\Delta y} - 2\phi_{x,y} + \phi_{x,y-\Delta y}}{\Delta y^2} + \frac{\rho}{\varepsilon_0} \quad (\text{A.21})$$

From this, a technique known as the *alternating-direction implicit* (ADI) method can be employed. In essence, the ADI method utilises a concept known as operator splitting, wherein the  $\frac{\partial^2 \phi}{\partial x^2}$  and  $\frac{\partial^2 \phi}{\partial y^2}$  terms can be decoupled, then each can be solved by iterating over half a time step. So for the first half time step, a pass is performed along the  $x$  direction; then at the second half time step, a pass is performed along the  $y$  direction as illustrated in figure A.5.

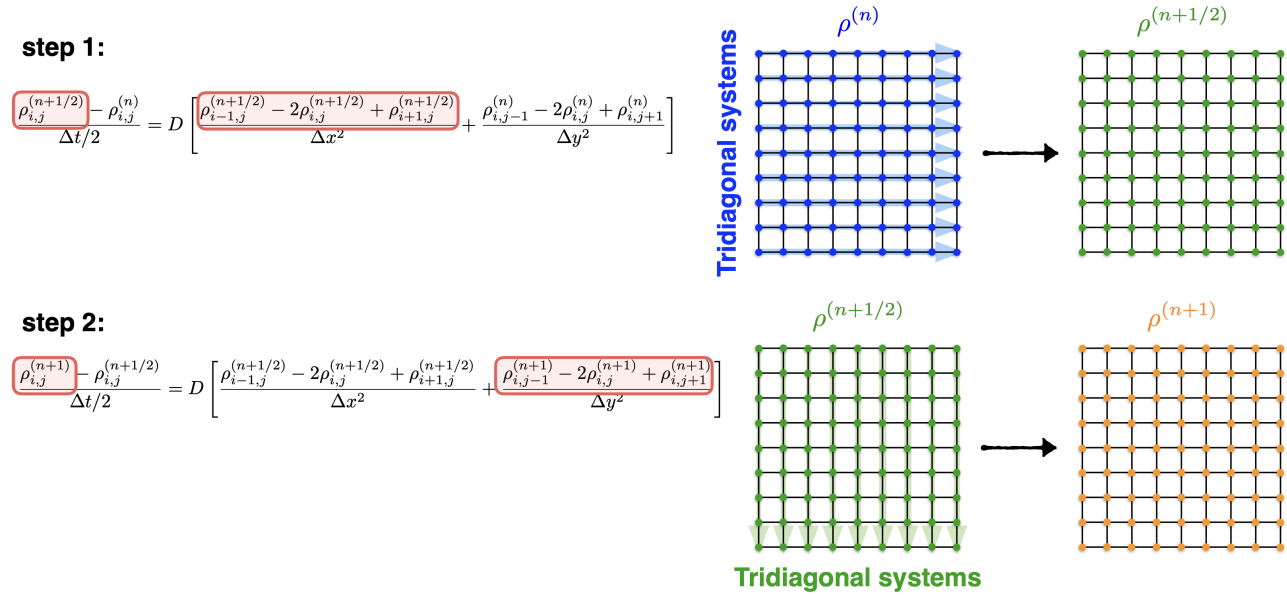


Figure A.5: Illustration of ADI method [32].

The benefit of this method is that rather than solving a large sparse matrix of a 2D system, a set of two independent 1D systems can be solved. These 1D systems can be arranged as a tridiagonal matrix, which can be efficiently solved using the *Thomas algorithm* [33].

Once the Poisson equation is solved and the potentials at the grid determined, the electric field

can be calculated again by the finite difference method. As the electric field is a vector, it needs to be calculated both along the direction of the  $x$ -axis and  $y$ -axis. Considering only the direction along the  $x$ -axis, equation A.22 can be used. For the case of a boundary, equation A.23 should be used instead.

$$E_x^{i,j} = \frac{\phi_{i+\Delta x,j} - \phi_{i-\Delta x,j}}{2\Delta x} \quad (\text{A.22})$$

$$E_x^{i,j} = \frac{\phi_{i+\Delta x,j} - \phi_{i,j}}{\Delta x} \quad (\text{A.23})$$

## A.4 Field Interpolation

The interpolation of the electromagnetic field values on the the particles is also performed using bilinear interpolation, however the reverse method to that done for the charge and current deposition. Therefore the electric field experienced by the particle is given by the contribution of the electric field vectors at each grid point.

Again, the general case seen in figure A.4 can be used. Here first step is to determine two intermediate points  $P_1$  and  $P_2$ :

$$P_1 = Q_{11} \frac{x_2 - x}{x_2 - x_1} + Q_{21} \frac{x - x_1}{x_2 - x_1} \quad (\text{A.24})$$

$$P_2 = Q_{12} \frac{x_2 - x}{x_2 - x_1} + Q_{22} \frac{x - x_1}{x_2 - x_1} \quad (\text{A.25})$$

Then, interpolate to the point of the particle  $Q$ :

$$Q = P_1 \frac{y_2 - y}{y_2 - y_1} + P_2 \frac{y - y_1}{y_2 - y_1} \quad (\text{A.26})$$

Thus for the fields, the variables  $Q$  would be replaced with the electric field vectors and the magnetic field vectors respectively. This process is repeated for all particles and the new electromagnetic field values are used in the particle mover for the next time step.

## A.5 Monte-Carlo Collisions

Steps 1-4 in figure A.1 are used to simulate collisionless plasma systems, where the charge particles kinetics are governed by magnetic interactions. However, when elastic and inelastic collisions between particles cannot be ignored, an additional step is sandwiched between steps 1 and 2 to account for this.

This is known as the *Monte-Carlo collision* (MCC) method, and it describes the collisions between the particles in a probabilistic fashion [34]. To start, the particles are evaluated for collisions. If a collision occurs, the particle velocity is updated in lieu with the type of collision. One potential downside to using the MCC method is that source particles collide with a target “cloud”, which is not a simulated particle. However, in practice the density of the background is significantly larger than the number of charged species being simulated, so this trade off is acceptable.

Determining if each and every particle in the simulation undergoes a collision can be very computationally expensive, as this requires the computation of each particles kinetic energy and their corresponding collision cross sections. Therefore, a computational trick is employed by adding an artificial collision term. The cross section of this term is chosen to force the total collision frequency for each species to be uniform and independent of the kinetic energy of the particle. This is called the *null collision* [34], which is illustrated in figure A.6.

From this, the portion of particles that should undergo a collision can be determined by the following expression [35]:

$$P(t) = 1 - e^{-\nu\Delta t} \quad (\text{A.27})$$

where  $\nu$  is the maximum of the sum of all collision frequencies. This can be expressed mathe-

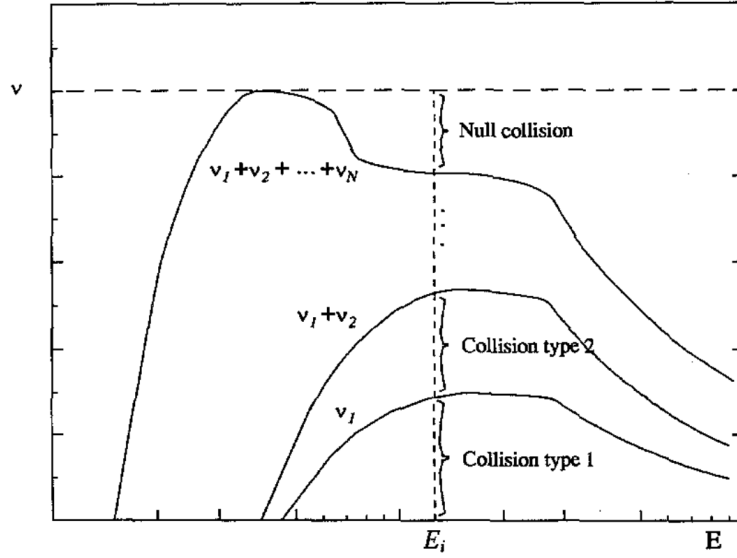


Figure A.6: Addition of null collision to produce a constant collision frequency across all energies [35].

matically as:

$$\nu = n_g \cdot \max(\sigma_{total}, v) \quad (\text{A.28})$$

where  $n_g$  is the neutral gas density (which can be assumed to be constant),  $\sigma_{total}$  is the total cross section from all collisions modelled (not including the null collision), and  $v$  is the relative speed between the colliding particle and the target.

Once the number of particles that experience collisions has been determined, particles are randomly picked from the population of simulated particles. This way, the kinetic energy of only a small subset of particles from the pool will be determined, making the simulation more efficient. Once a particle has been chosen and its kinetic energy calculated, a random number between  $[0, 1]$ , called  $R$ , is selected. This is used to determine the collision type for the particle, as a function of the value of  $R$ , as shown by table A.1.

Table A.1: Determining the type of collision based on the value of  $R$  [35].

	$R \leq \nu_1/\nu$	Collision Type 1
$\nu_1/\nu < R \leq (\nu_1 + \nu_2)/\nu$		Collision Type 2
	$\vdots$	
$(\nu_1 + \nu_2 + \dots + \nu_n)/\nu < R$		Null Collision

If the collision type selected is a null collision, then it is treated as no collision occurred.

# Appendix B

## XOOPIC

The PIC simulation program used in this project is called *X11 object-oriented particle-in-cell* (XOOPIC). It is a C/C++ based program that simulates 2D plasma systems. It was originally developed in the 1990s by the Plasma Theory and Simulation Group from the University of California at Berkley [36]. The code base was subsequently forked by the Plasma and Pulsed Power Group at Loughborough University, and improved upon to include additional features and output diagnostics for analysis.

### B.1 Overview

XOOPIC is primarily a command-line-interface (CLI) program but support X11 windowing to visualise certain diagnostics in real time. Some examples of these real time diagnostics include: average kinetic energies of the particles, phase-space plots of the position and velocities of the various particle species, and the electric field vectors at the simulation grid. While important for determining the behaviour of the plasma system, running the simulation with these windows does significantly reduce its performance. Therefore, XOOPIC's in-built visualisations are primarily used to observe the snapshot behaviour of the simulated system, whilst any diagnostic information required for further analysis is typically written into output files.

Despite not running with X11 windowing, running these simulations continuously takes a long

period of time (typically on the order of days to weeks) before they settle into a steady state. This is because the simulations have to be run at very small time steps in order to be stable (see section 4.1.2).

### B.1.1 Remote Server

Due to this long simulation time, running XOOPIC simulations continuously on a local machine are just not feasible. Instead, simulations are run remotely on Loughborough University’s high performance servers via *secure shell* (SSH). Typically, multiple simulations are run concurrently in order to test various model parameters.

There are several risks associated with running simulations using a remote server. The first being that if (and when) the connection between the client and the server is severed, the simulations will be killed by the server. This problem can be alleviated with the use of terminal multiplexors, such as *GNU Screen*<sup>1</sup>. This allows for the creation of multiple pseudo-terminal sessions that run in the background. Once created, the client is free to attach and detach sessions without the need for an uninterrupted connection to the server.

A broken client-server connection is not the only way a simulation can be terminated. Some others include unexpected server restarts, power outages, or overuse of server resources due to memory leaks. In such cases, the simulation can be resumed using XOOPIC’s dump files (also referred to as restart files). These files are essentially periodic saves of the simulations and can be used to restart the simulation from the last save point if the need arises. The save interval between dump files is set when starting the simulation. Though tempting to set this interval as small as possible in order to mitigate any data loss, generating these files is very expensive computationally as it involves writing most of the simulation variables onto disk. Thus, the dump file interval are set in the neighbourhood of hundreds of thousands of time steps.

---

<sup>1</sup><https://www.gnu.org/software/screen/>

### B.1.2 Input Files

The parameters for XOOPIC's simulations are set using an input file. This is simply a custom formatted text file, with a pseudo-JSON-like structure. The input file is divided into three sections: headers, variables, and region. The first two sections are for the user's benefit, describing the simulation and the parameter values used respectively.

The region section however is where the true simulation parameters are specified. It can be further sub-divided into multiple subsections. The list of all possible subsections is vast, though a typical PIC simulation includes:

- **Grid** where the dimensions of the plasma device are specified, either in cylindrical or cartesian geometry.
- **Control** where the control parameters such as the size of the time step or a flag to use a specific field solver are set.
- **Species** which state parameters of the particle species being simulated, for example its mass and charge.
- **MCC** that determine the collision characteristics of the plasma based on the background gas pressure and temperature. The collisions can also be turned off outright.
- **Load** that establishes the region in which the particle species are loaded.
- **Diagnostic** which as the name suggests extracts the various diagnostic information and saves them to an output file.

The other subsections not listed are the various boundary parameters. The usage of these parameters will vary based on the type of device being simulated. Some examples of boundary parameters include: a grounded boundary, a current source, and a dielectric boundary.

When constructing the input files, care must be taken to ensure that the grid size (within the grid subsection) and the time step (within the control subsection) obey a set of conditions so that the simulation is stable.

The grid size of the simulation,  $\Delta x$  and  $\Delta y$  should adhere to the equation [26]:

$$\Delta x < 3.4\lambda_D \quad (\text{B.1})$$

where  $\lambda_D$  is the Debye length. This is to ensure that the electric fields in the sheath can be resolved.

As for the time step,  $\Delta t$ , it should be able to resolve the plasma oscillations, thus should satisfy the equation [37]:

$$\Delta t < 0.2\omega_{pe}^{-1} \quad (\text{B.2})$$

where  $\omega_{pe}$  is the plasma frequency. Note, this condition is only valid for electrostatic plasma simulations.

## B.2 Improvements

During the course of this project, several improvements were made to XOOPIC. This primarily included bug fixes, but also the inclusion of a new boundary parameter (within the region section) called the *Circuit* boundary.

### B.2.1 Motivation

XOOPIC previously had two types of (traditional) input source boundaries. An ideal voltage source, known as the *Equipotential* boundary; and an ideal current source, called the *Current Source* boundary.

With the Equipotential boundary, the simulation always keeps the potential at the boundary equal to the source voltage specified in the input file. This has the issue where there are no maximum or minimum bounds for current through the boundary. Thus, theoretically the current through the boundary can grow exponentially to infinity. In practice however, the simulation



simply becomes unstable and crashes. It is also possible for this current to exceed the rated current of the intended power supply to be used.

Likewise with the Current Source boundary, the simulation attempts to keep the current across the boundary at a constant specified value; despite the potential at the boundary. And in practice, it is possible that the potential produced by the simulation exceeds the voltage that can be delivered by the power supply.

Hence, in order to accurately simulate a “real world” power supply, the Circuit boundary was introduced. This boundary represents the configuration of an ideal voltage source with a resistor attached in series. An illustration of this can be seen in figure B.1. The one significant assumption with this boundary is that the circuit shares the same ground plane as the rest of the plasma device being simulated, which is normally the case.

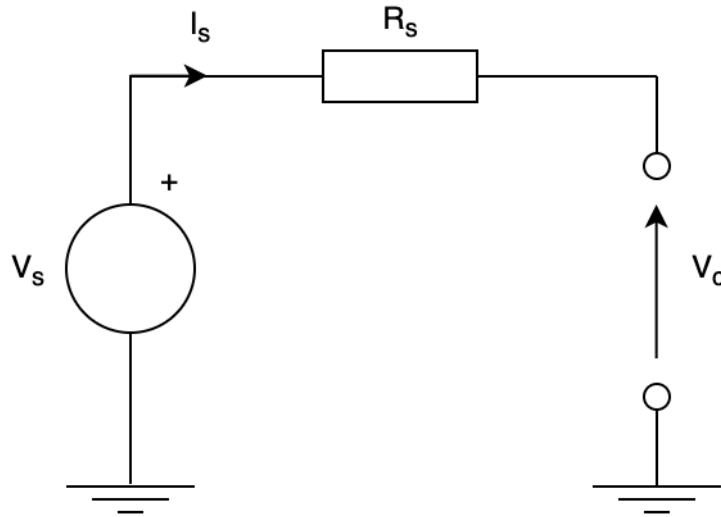


Figure B.1: Illustration of circuit boundary.

By adding the series resistor, in effect the maximum voltage and current across the boundary has been limited. As seen in figure B.2, the maximum voltage is obtained when the simulated device is an open circuit. As for the maximum current, it is achieved when the simulated device behaves as a short circuit. Thus the potential of the Circuit boundary can be given by:

$$V_c = V_s - I_s R_s \quad (\text{B.3})$$

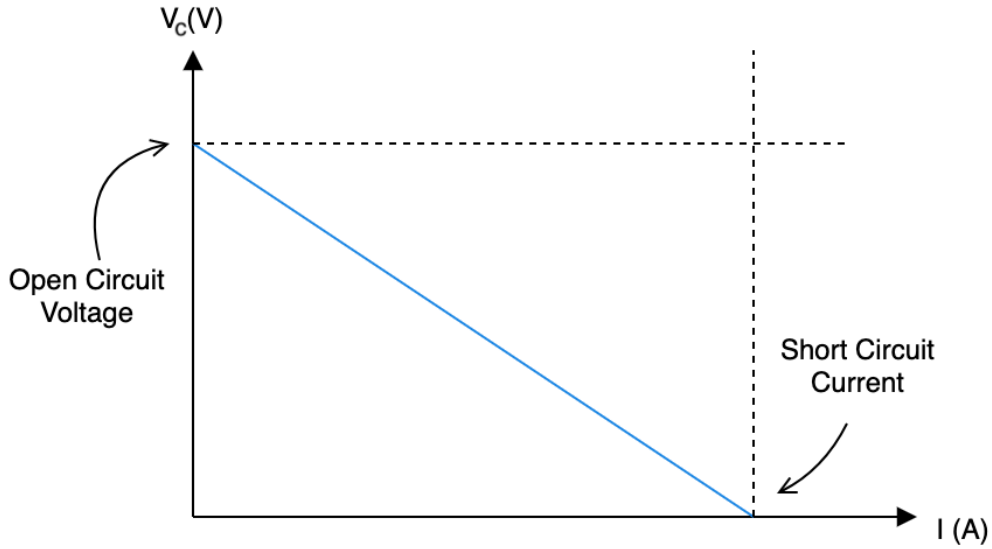


Figure B.2: Voltage-current relationship of circuit boundary.

### B.2.2 Methodology

As mentioned previously, XOOPIC has the capability of performing simulations in cartesian geometry or cylindrical geometry. Hence an implementation was required for both geometry types. For this report, a general solution based on [38, 39] is first described, followed by the specific coefficient values required in either geometry.

#### General Solution

A case for the Circuit boundary shown in figure B.3. The points represent an arbitrary fixed grid, with grid points labelled  $i$  and  $j$  that correspond to the relative positions along the horizontal and vertical directions respectively. The boundary itself is represented by the vertical line, placed along the left most grid points, where  $i = 0$ .

The potential at each grid point that intersects the boundary is first taken, then these values are averaged to give the potential of the overall Circuit boundary. For a given point along the boundary, the potential can be computed using Gauss's law.

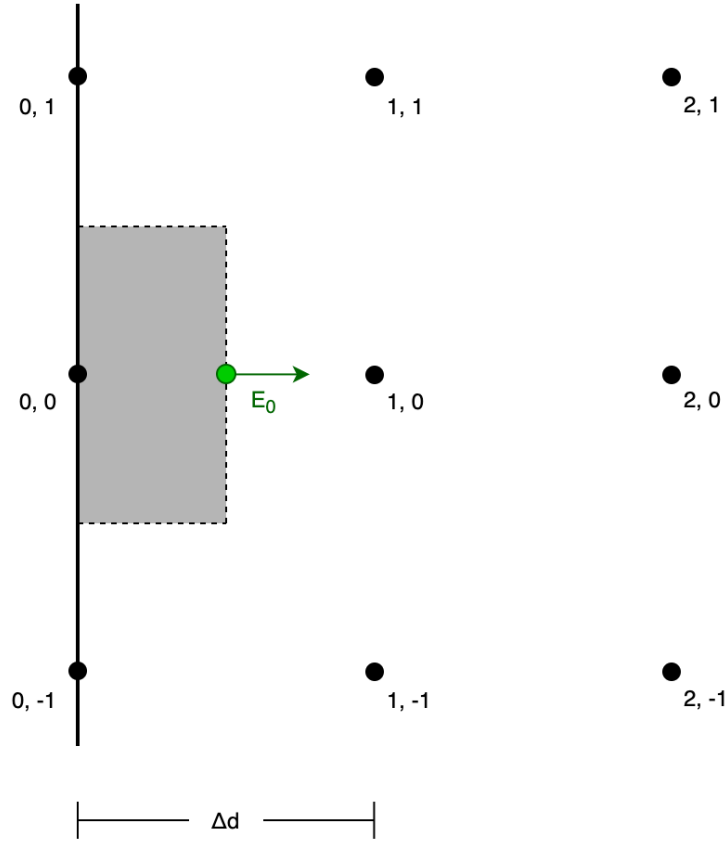


Figure B.3: Illustration of a circuit boundary along a fixed grid.

The expression for a Gaussian pillbox (shown by the dashed line in figure B.3) is:

$$\oint_S E \cdot dS = \frac{Q}{\varepsilon_0} \quad (\text{B.4})$$

where  $Q$  is the charge enclosed by said pillbox. This charge can be expressed as a sum of the volume charge within the pillbox and the surface charge at the boundary:

$$Q = \oint_V \rho \cdot dV + \oint_S \sigma \cdot dS \quad (\text{B.5})$$

Combining equations B.4 and B.5, then integrating over their respective areas and volumes results in the expression:

$$E \cdot A_1 = \frac{1}{\varepsilon_0} (\rho \cdot V + \sigma \cdot A_2) \quad (\text{B.6})$$

Note that there are two different areas produced: one related to the surface charge density along the boundary,  $A_2$ ; and one related to electric field out of the pillbox,  $A_1$ . The values of

these terms depend on the geometry used.

The electric field can be expressed in terms of the potential difference:

$$E = -\nabla\phi \quad (\text{B.7})$$

Thus, the forward-difference method can be used to determine the electric field of the pillbox seen in figure B.5.

$$\frac{\phi_0 - \phi_1}{\Delta d} \cdot A_1 = \frac{1}{\varepsilon_0}(\rho \cdot V + \sigma \cdot A_2) \quad (\text{B.8})$$

An additional note regarding equation B.8, the term  $\Delta d$  denotes the distance between the grid points. Similarly to the area and volume terms, this value depends on the geometry used.

As explained in chapter 3, the volume charge densities of particles within PIC simulations are discretised onto the grid using bilinear interpolation. This means the the volume charge of the pillbox is known at the at the grid. Therefore, the only unknown term on the RHS of equation B.8 is the surface charge density.

This can be determined using Kirchoff's current law in the circuit shown in figure B.1:

$$\frac{d\sigma}{dt} = J_{cond} + J_{conv} \quad (\text{B.9})$$

Equation B.9 can be expressed numerically using the backwards-difference method. Additionally, the conduction and convection current density can expressed in terms of their charges, eliminating the  $dt$  terms on both sides.

$$\sigma^t - \sigma^{t-\Delta t} = \frac{1}{A_2} (Q^t - Q^{t-\Delta t} + Q_{conv}) \quad (\text{B.10})$$

The variables  $\sigma^{t-\Delta t}$  and  $Q^{t-\Delta t}$  represent quantities determined in the previous time step, thus should be known. Supposing it is the start of the simulation where  $t = 0$ , they can be simply initialised to zero.  $Q_{conv}$  represents the charge deposited onto the boundary by particles since the previous time step. Hence the only unknown term on the RHS of equation is the conduction

charge at the current time step,  $Q^t$ .

This conduction charge can be determined using Kirchoff's voltage law (also expressed in equation B.3, though in a slightly different form):

$$\phi_0 = V_s - \frac{dQ}{dt} \cdot R_s \quad (\text{B.11})$$

The derivative term can again be solved numerically using the backwards-difference. However unlike the other equations, a second order difference is used here to provide a better approximation of the charge. This second order backwards-difference is given as:

$$\frac{dQ}{dt} = \frac{3Q^t - 4Q^{t-\Delta t} + Q^{t-2\Delta t}}{2\Delta t} \quad (\text{B.12})$$

Combining equations B.11 and B.12 provides a new expression for the conduction charge,  $Q^t$ :

$$Q^t = \frac{V_s - \phi_0 - (\alpha_1 Q^{t-\Delta t} + \alpha_2 Q^{t-2\Delta t})}{\alpha_0} \quad (\text{B.13})$$

where  $\alpha_0 = \frac{3}{2} \frac{R_s}{\Delta t}$ ,  $\alpha_1 = 2 \frac{R_s}{\Delta t}$ , and  $\alpha_2 = \frac{1}{2} \frac{R_s}{\Delta t}$  are constants to simplify the expression.

Using equation B.13, a new surface charge density expression can be determined:

$$\sigma^t - \sigma^{t-\Delta t} = \frac{1}{A_2} \left( \frac{V_s - \phi_0 - (\alpha_1 Q^{t-\Delta t} + \alpha_2 Q^{t-2\Delta t})}{\alpha_0} - Q^{t-\Delta t} + Q_{conv} \right) \quad (\text{B.14})$$

This in turn can be combined with equation B.8 from Gauss's law to give the expression:

$$\frac{\phi_0 - \phi_1}{\Delta d} \cdot A_1 + \frac{\phi_0}{\alpha_0 \varepsilon_0} = \frac{1}{\varepsilon_0} \left( \rho \cdot V + \sigma^{t-\Delta t} \cdot A_2 + \left( \frac{V_s - K^t}{\alpha_0} - Q^{t-\Delta t} + Q_{conv} \right) \right) \quad (\text{B.15})$$

where  $K^t = \alpha_1 Q^{t-\Delta t} + \alpha_2 Q^{t-2\Delta t}$ . Note, that the unknown terms ( $\phi_0$  and  $\phi_1$ ) have been rearranged to the LHS of the equation.

Typically, the coefficients in equation B.15 can then be fed into the field solver to determine the potential of all grid points. However in XOOPIC, the grid potentials of each boundary

within the simulation are individually computed before the simulation begins. Then at each time step, the overall potential is determined by summing the predetermined potential induced by the individual boundaries via superposition, and adding the potential due to space charges (from the particles). This approach does not necessarily speed up the computation of the field solver, however it does decouple the boundary code from the field solver code; making it easier to implement new boundaries.

Because of this pre-computation, equation B.15 can be simplified by specifying  $\phi_1 = c_1\phi_0$ , where  $c_1$  is the ratio of  $\phi_1/\phi_0$ . Hence, the general solution for a circuit boundary can be given as:

$$\phi_0 \left( (1 - c_1)A_1 + \frac{\Delta d}{\alpha_0 \varepsilon_0} \right) = \frac{\Delta d}{\varepsilon_0} \left( \rho \cdot V + \sigma^{t-\Delta t} \cdot A_2 + \left( \frac{V_s - K^t}{\alpha_0} - Q^{t-\Delta t} + Q_{conv} \right) \right) \quad (\text{B.16})$$

### Cartesian Geometry

There are two possible orientations for the Circuit boundary for the cartesian geometry: along (or parallel to) the  $x$ -axis, or along the  $y$ -axis. Therefore, the variables seen in the left most column of table B.1 should be replaced by their values in the given orientation of the Circuit boundary.

Table B.1: Circuit boundary variables for cartesian geometry.

Variables	Along $x$ -axis	Along $y$ -axis
$\Delta d$	$\Delta y$	$\Delta x$
$A_1$	$\Delta x \Delta z$	$\Delta y \Delta z$
$A_2$	$\Delta x \Delta z$	$\Delta y \Delta z$
$V$	$\Delta x \Delta y \Delta z$	$\Delta y \Delta y \Delta z$

When operating in the cartesian coordinate system, the two area terms  $A_1$  and  $A_2$  are identical irregardless of the orientation.

## Cylindrical Geometry

The two possible orientations for a cylindrical geometry are: along the  $r$ -axis, or along the  $z$ -axis. However, unlike the cartesian geometry where  $A_1$  always equals  $A_2$  for both orientation, this only holds for the case where the Circuit boundary is along the  $r$ -axis. For the case along the  $z$ -axis,  $A_1$  and  $A_2$  are distinct.

The terms for a given orientation of the Circuit boundary in cylindrical geometry can be seen in table B.2.

Table B.2: Circuit boundary variables for cylindrical geometry.

Variables	Along $z$ -axis	Along $r$ -axis
$\Delta d$	$\Delta r$	$\Delta z$
$A_1$	$2\pi r_{i+0.5\Delta r}\Delta z$	$\pi(r_{j+0.5\Delta r}^2 - r_{j-0.5\Delta r}^2)$
$A_2$	$2\pi r_i\Delta z$	$\pi(r_{j+0.5\Delta r}^2 - r_{j-0.5\Delta r}^2)$
$V$	$\pi(r_{i+0.5\Delta r}^2 - r_i^2)\Delta z$	$\frac{1}{2}\pi(r_{j+0.5\Delta r}^2 - r_{j-0.5\Delta r}^2)\Delta z$

### B.2.3 Validation

The validation for the Circuit boundary was done in two parts. The first was a test case without particles, which was then followed by one with particles. The former was used to evaluate the accuracy of the boundary calculations itself, without the computation from particles (i.e. the discretisation of the volume charge densities or the count of the number of particles colliding with the boundary). The latter was to test the operation of the boundary in a simulation scenario, which almost always has particles.

For both test cases, only simulation of a device in cartesian geometry is shown for the sake of brevity and the fact that the solution to the potential of the circuit boundary is highly dependant on the geometry (as discussed in the previous subsection).

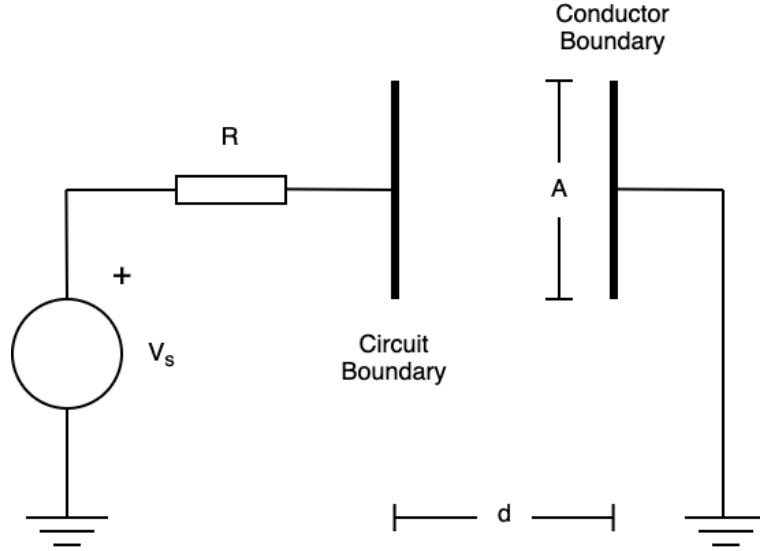


Figure B.4: Illustration of test case for Circuit boundary without particles.

### Test Case without Particles

An illustration of the device being simulated can be seen in figure B.4, where the Circuit boundary was placed along the  $y$ -axis at the left-most wall and a grounded *Conductor* boundary placed along the right-most wall. This device, without any particles, essentially behaves as a capacitor with a capacitance given by  $C = \frac{\epsilon_0 A}{d}$ . The parameters for this test case can be found in table B.3

Table B.3: Parameters for test case of Circuit boundary without particles.

Parameters	Values
$V_s$	1000 V
$R$	1000 $\Omega$
$A$	0.05 m <sup>2</sup>
$d$	0.05 m
$C$	8.85 pF

Thus, this simulation models the charging of a capacitor in an  $RC$  circuit, which can be expressed as:

$$V_c = V_s(1 - e^{-t/\tau}) \quad (\text{B.17})$$

where the time constant is  $\tau = RC$ .

For the simulated device,  $C = 8.85$  pF and  $\tau = 8.85$  ns. From this, an analytical solution can



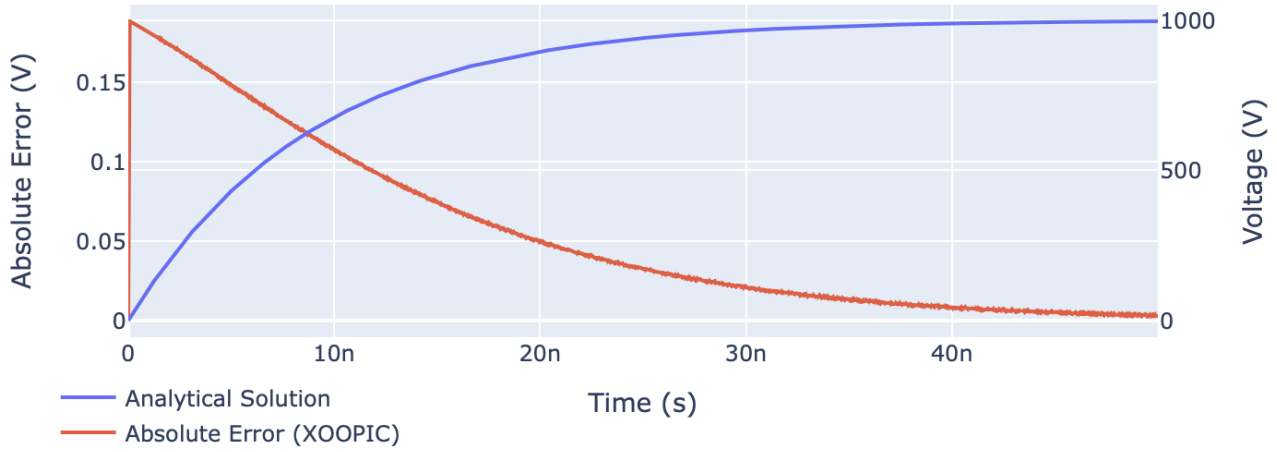


Figure B.5: Comparison between the analytical solution and XOOPIC, where  $\Delta t = 10$  ps.

be determined, with the RC curve shown in figure B.5. For the XOOPIC simulation, a run was performed from  $t = 0$  to  $t = 50$  ns (approximately 5 time constants), with a time step of  $\Delta t = 10$  ps. The resulting RC curve overlapped the the one produced by the analytical solution, hence only the absolute error is shown.

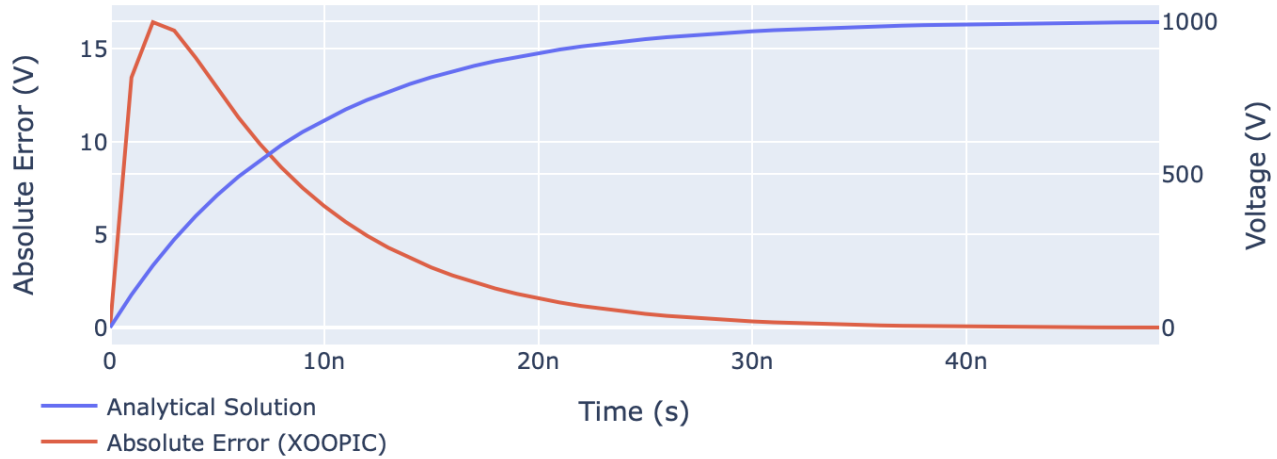


Figure B.6: Comparison between the analytical solution and XOOPIC, where  $\Delta t = 1$  ns.

This error seen is a convergence error, which is due to the conduction charge values requiring a finite number of iterations before they converge to the true value. To illustrate this, the same simulation is run with a larger time step of  $\Delta t = 1$  ns (100 times that of the original simulation). These results can be seen in figure B.6. Notice that there is a significantly larger absolute error (nearly 100 times greater). However when observing the percentage error, seen in figure B.7, the differences are quite comparable. Therefore, so long as the time step used is sufficiently small (to ensure a small absolute error), the simulations can be said to be accurate

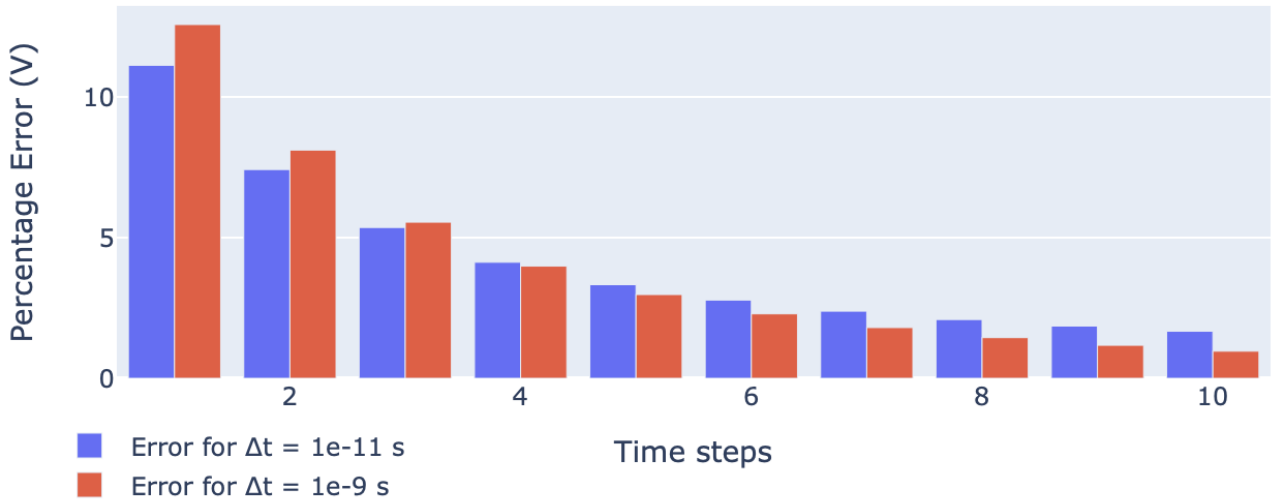


Figure B.7: Comparison of the error from XOOPIC when  $\Delta t = 10$  ps and  $\Delta t = 1$  ns.

enough.

### Test Case with Particles

Generating a simplified test case to only asses the impact of particles on the Circuit boundary was slightly more challenging. The simulated circuit for this test case can be seen in figure B.8. As for the parameters used, they can be found in table B.4.

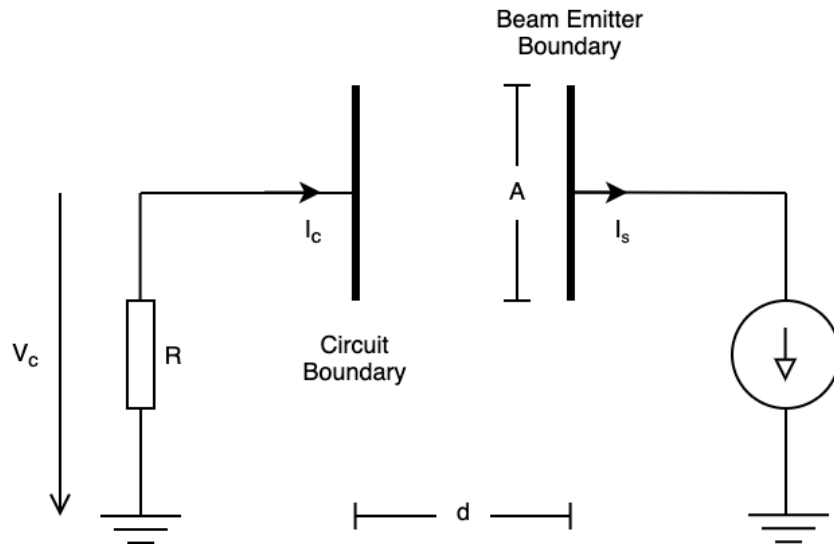


Figure B.8: Illustration of test case for Circuit boundary without particles.

Notice that the grounded Conductor boundary was replaced with a *Beam Emitter* boundary. The Beam Emitter is similar to the Current Source boundary, wherein a steady supply of charge

Table B.4: Parameters for test case of Circuit boundary with particles.

Parameters	Values
$V_s$	0 V
$I_s$	1 A
$R$	1000 $\Omega$
$A$	$5 \times 10^{-4}$ m <sup>2</sup>
$d$	$5 \times 10^{-4}$ m
$C$	8.85 pF
$v_{d,x}$	1000 eV
$v_{d,y}$	0 eV

is supplied to the boundary. However, unlike the Current Source which simply deposits the charge at the boundary (which in turn generates a potential), the Beam Emitter releases this charge into the simulation domain in the form of particles. This steady source of particles is what enabled the evaluation of this test case. The particles emitted out of the Beam Emitter (i.e. towards the LHS) in this case were electrons, hence why source current  $I_s$  is shown in the opposite direction. To ensure no particle losses, collisions by the MCC were turned off, the simulated device was set to a vacuum, and the drift velocity of the particles along the  $y$ -axis,  $v_{d,y}$  was set to 0 eV.

As for the Circuit boundary itself, the source voltage  $V_s$  was grounded, implying that the potential of the boundary is solely given by the current through the resistor,  $I_c$ . Additionally, because the source current must be equal to the circuit current (as there were no losses) and one end of the resistor was grounded, the potential at the Circuit boundary has to be negative.

The analytical solution for this test case is given by the conduction current from electrons colliding with the Circuit boundary, and the displacement current across the capacitor. The conduction current is merely a step from 0 A to the  $-1$  A specified by the source current. It is negative because the current is leaving the boundary. The time at which this step occurs is given by the time taken for the electrons to travel across the device. As the drift velocity of the electrons along the direction of the  $x$ -axis was set to  $v_{d,x} = 1000$  eV, thus its true velocity can be determined using the equation for kinetic energy:

$$E_{ke} = \frac{1}{2}mv^2 \quad (\text{B.18})$$

where  $1 \text{ eV} = 1.6 \times 10^{-19} \text{ J}$ .

This resulted in a velocity of approximately  $1.87 \times 10^7 \text{ ms}^{-1}$ , hence it crossed the length of the device in roughly 30 ps. Thus this is when the step in conduction current should occur.

As for the displacement current, this is given by:

$$I_{disp} = C \frac{dV}{dt} \quad (\text{B.19})$$

Combining this with the analytical solution of the RC circuit in equation B.17, gives the displacement current of:

$$I_{disp} = \frac{V_{ss}}{R} e^{-\frac{t}{\tau}} \quad (\text{B.20})$$

where  $V_{ss}$  is the potential difference across the capacitor when it reaches a steady state, which is given as  $V_{ss} = I_s R$ . The displacement current is in opposite the opposite direction to the conduction current, hence in this case it is positive. Similiarly to the conduction current, the displacement current at the surface of the Circuit boundary would only occur after the electrons collide with the boundary itself.

The overall potential is obtained by combining the contributions of the conduction and displacement currents with the resistance of the circuit. This is expressed in the equation below, and is illustrated in figure B.9.

$$V_c = \begin{cases} 0 & t < 30 \text{ ps} \\ I_s R (e^{-\frac{t}{\tau}} - 1) & t \geq 30 \text{ ps} \end{cases} \quad (\text{B.21})$$

For the simulation, a similar overall device geometry was used to that of the the previous test, however the gap distance  $d$  was decreased to minimise the time required for the electrons to collide with the boundary. This meant that the area of the boundary plates  $A$  also had to be decreased to ensure that the capacitance, and by extension the time constant, remained the same. Again, the simulations were run from  $t = 0$  to  $t = 50 \text{ ns}$ , with a time step of  $\Delta t = 10 \text{ ps}$ . Figure B.9 also shows the absolute error of the Circuit boundary of the simulation as apposed

to that of the analytical solution. The error observed is much larger with a maximum error of approximately 26 V; quite a significant error. However, at the time of writing this report, the origin of this error is still unknown.

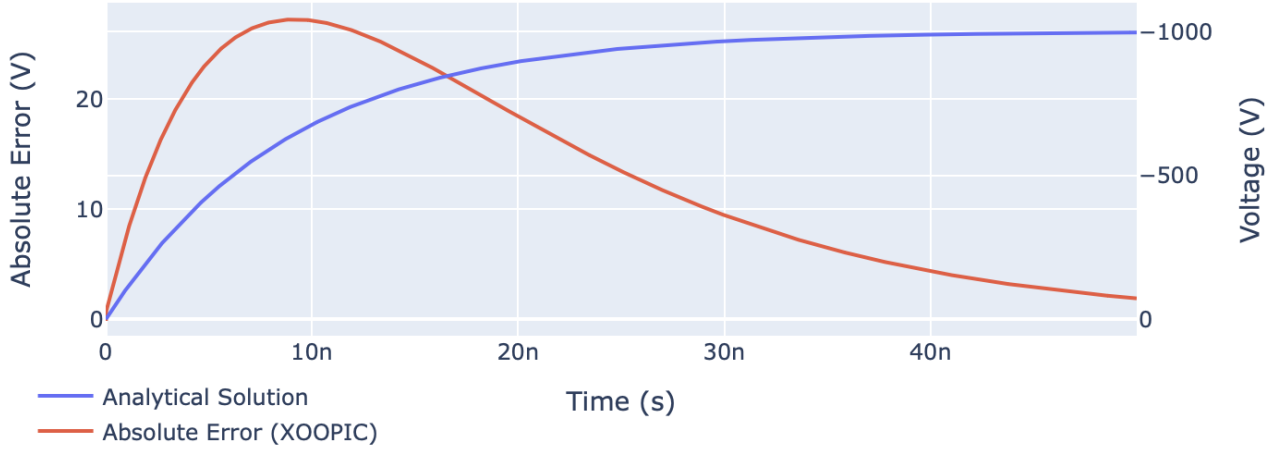


Figure B.9: Illustration of test case for Circuit boundary without particles.

### B.2.4 Future Work

Aside from the Circuit boundary simulating a more accurate “real world” voltage source, it can possibly be used in model more complicated circuit networks. This is because, Thevenin’s theorem dictates that any linear circuit network can be represented by an equivalent circuit that contains a voltage source with a series impedance (which is a resistance in this case).

Nonetheless, most circuits also contain some amount of capacitance and/or inductance. Hence, it could potentially be beneficial to add a series inductor and capacitor to the Circuit boundary in addition to the existing resistor. To achieve this, the the RHS of Kirchoff’s voltage law, equation B.11, needs to be modified to include the potential due to the inductor,  $V = \frac{d^2Q}{dt^2}L$ , and the potential due to a capacitor,  $V = \frac{Q}{C}$ . This new equation can be rearranged to solve for the current conduction charge. From there, the same process can be applied to determine the potential of the Circuit boundary.

# Bibliography

- [1] IPCC, “Climate change: a threat to human wellbeing and health of the planet. taking action now can secure our future — IPCC,” Feb 2022.
- [2] “Inventory of u.s. greenhouse gas emissions and sinks — US EPA, url=<https://www.epa.gov/ghgemissions/inventory-us-greenhouse-gas-emissions-and-sinks>, journal=US EPA, author=EPA, year=2019, month=Apr.”
- [3] H. Ritchie and M. Roser, “CO<sub>2</sub> and greenhouse gas emissions,” *Our World in Data*, May 2020.
- [4] M. B. Ross, P. De Luna, Y. Li, C.-T. Dinh, D. Kim, P. Yang, and E. H. Sargent, “Designing materials for electrochemical carbon dioxide recycling,” *Nature Catalysis*, vol. 2, p. 648–658, Jul 2019.
- [5] U. Arnold, T. Brück, A. De Palmenaer, and K. Kuse, “Carbon capture and sustainable utilization by algal polyacrylonitrile fiber production: Process design, techno-economic analysis, and climate related aspects,” *Industrial and Engineering Chemistry Research*, vol. 57, p. 7922–7933, May 2018.
- [6] M. A. Lieberman and A. J. Lichtenberg, *Principles of Plasma Discharges and Materials Processing: Second Edition*. Wiley-Interscience, 2005.
- [7] J. T. Gudmundsson and A. Hecimovic, “Foundations of DC plasma sources,” vol. 26, p. 123001, nov 2017.
- [8] C. F. Gallo, “Coronas and Gas Discharges in Electrophotography:A Review,” *IEEE Transactions on Industry Applications*, vol. IA-11, no. 6, pp. 739–748, 1975.

- [9] A. Bogaerts, E. Neyts, R. Gijbels, and J. Van der Mullen, “Gas discharge plasmas and their applications,” *Spectrochimica Acta Part B: Atomic Spectroscopy*, vol. 57, pp. 609–658, apr 2002.
- [10] P. Chabert and N. Braithwaite, *Physics of radio-frequency plasmas*, vol. 9780521763. Cambridge University Press, jan 2011.
- [11] T. D. Chu, “High Frequency Breakdown Voltage,” Tech. Rep. March, Superconducting Super Collider Project Office, mar 1992.
- [12] J. Pim, “The electrical breakdown strength of air at ultra-high frequencies,” *Proceedings of the IEE - Part III: Radio and Communication Engineering*, vol. 96, pp. 117–129, mar 1949.
- [13] S. Rayne, “Thermal carbon dioxide splitting: A summary of the peer-reviewed scientific literature,” *Nature Precedings*, Apr 2008.
- [14] Z. Jiang, T. Xiao, V. L. Kuznetsov, and P. P. Edwards, “Turning carbon dioxide into fuel,” *Philosophical Transactions of the Royal Society A: Mathematical, Physical and Engineering Sciences*, vol. 368, p. 3343–3364, Jul 2010.
- [15] R. Snoeckx and A. Bogaerts, “Plasma technology-a novel solution for CO<sub>2</sub> conversion?,” oct 2017.
- [16] D. Pakhare and J. Spivey, “A review of dry (co<sub>2</sub>) reforming of methane over noble metal catalysts,” *Chem. Soc. Rev.*, vol. 43, p. 7813–7837, Feb 2014.
- [17] 2011.
- [18] U. Kogelschatz, “Dielectric-barrier discharges: Their history, discharge physics, and industrial applications,” *Plasma Chemistry and Plasma Processing*, vol. 23, no. 1, p. 1–46, 2003.
- [19] L. F. Spencer and A. D. Gallimore, “Efficiency of co<sub>2</sub> dissociation in a radio-frequency discharge,” *Plasma Chemistry and Plasma Processing*, vol. 31, p. 79–89, Nov 2010.

- [20] H. Xu, M. Shaban, S. Wang, A. Alkayal, D. Liu, M. G. Kong, F. Plasser, B. R. Buckley, and F. Iza, “Oxygen harvesting from carbon dioxide: simultaneous epoxidation and CO formation,” *Chemical Science*, 2021.
- [21] R. A. Dextre and K. G. Xu, “Effect of the Split-Ring Resonator Width on the Microwave Microplasma Properties,” *IEEE Transactions on Plasma Science*, vol. 45, pp. 215–222, feb 2017.
- [22] H. Wheeler, “Transmission-line properties of a strip on a dielectric sheet on a plane,” *IEEE Transactions on Microwave Theory and Techniques*, vol. 25, p. 631–647, Aug 1977.
- [23] H. C. Kim, F. Iza, S. S. Yang, M. Radmilović-Radjenović, and J. K. Lee, “Particle and fluid simulations of low-temperature plasma discharges: benchmarks and kinetic effects,” *Journal of Physics D: Applied Physics*, vol. 38, p. R283, sep 2005.
- [24] D. Tskhakaya, K. Matyash, R. Schneider, and F. Taccogna, “The Particle-In-Cell Method,” *Contributions to Plasma Physics*, vol. 47, pp. 563–594, dec 2007.
- [25] C. K. Birdsall, “Particle-in-Cell Charged-Particle Simulations, Plus Monte Carlo Collisions With Neutral Atoms, PIC-MCC,” *IEEE Transactions on Plasma Science*, vol. 19, no. 2, pp. 65–85, 1991.
- [26] R. Hockney and J. Eastwood, *Computer Simulation Using Particles*. CRC Press, mar 1988.
- [27] A. T. Gisbert and N. Piovella, “Multimode collective atomic recoil lasing in free space,” *Atoms*, vol. 8, p. 93, Dec 2020.
- [28] C. K. Birdsall and A. B. Langdon, *Plasma physics via computer simulation*. CRC Press, 1st ed ed., oct 2004.
- [29] W. H. Press, B. P. Flannery, S. A. Teukolsky, and W. T. Vetterling, *Numerical Recipes in C: The Art of Scientific Computing*. Cambridge University Press, 1988.
- [30] S. V.-U. Ha, T.-A. Vu, and H. M. Tran, “An Extended Occlusion Detection Approach for Video Processing,” *REV Journal on Electronics and Communications*, vol. 8, jan 2019.



- [31] W. H. Press, B. P. Flannery, S. A. Teukolsky, and W. T. Vetterling, *Numerical Recipes in C: The Art of Scientific Computing*. Cambridge University Press, 1988.
- [32] F. Wermelinger, “Diffusion with Alternating Direction Implicit (ADI) and Particle Strength Exchange (PSE) methods.”
- [33] W. H. Press, B. P. Flannery, S. A. Teukolsky, and W. T. Vetterling, *Numerical Recipes in C: The Art of Scientific Computing*. Cambridge University Press, 1988.
- [34] F. Iza, S. H. Lee, and J. K. Lee, “Computer modeling of low-temperature plasmas,” *Transworld Research Network*, vol. 37, no. 2, 2007.
- [35] V. Vahedi and M. Surendra, “A Monte Carlo collision model for the particle-in-cell method: applications to argon and oxygen discharges,” *Computer Physics Communications*, vol. 87, pp. 179–198, may 1995.
- [36] J. P. Verboncoeur, A. B. Langdon, and N. T. Gladd, “An object-oriented electromagnetic PIC code,” *Computer Physics Communications*, vol. 87, pp. 199–211, may 1995.
- [37] D. Tskhakaya, K. Matyash, R. Schneider, and F. Taccogna, “The particle-in-cell method,” *Contributions to Plasma Physics*, vol. 47, p. 563–594, Dec 2007.
- [38] J. P. Verboncoeur, M. V. Alves, V. Vahedi, and C. K. Birdsall, “Simultaneous Potential and Circuit Solution for 1D Bounded Plasma Particle Simulation Codes,” *Journal of Computational Physics*, vol. 104, pp. 321–328, feb 1993.
- [39] V. Vahedi and G. Dipeso, “Simultaneous Potential and Circuit Solution for Two-Dimensional Bounded Plasma Simulation Codes,” *Journal of Computational Physics*, vol. 131, pp. 149–163, feb 1997.